Journal of Geophysical Research: Space Physics

RESEARCH ARTICLE
10.1029/2018JA025387

Solar Wind and Seasonal Influence on Ionospheric Currents From Swarm and CHAMP Measurements

K. M. Laundal[1], **C. C. Finlay**[2], **N. Olsen**[2], **and J. P. Reistad**[1]

[1] Birkeland Centre for Space Science, Department of Physics and Technology, University of Bergen, Bergen, Norway, [2] DTU Space, National Space InstituteTechnical University of Denmark, Kgs. Lyngby, Denmark

Key Points:
- We present a new global model of the full ionospheric current system based on magnetic field measurements from LEO by Swarm and CHAMP
- The horizontal current is confined to the auroral oval in the winter, and it connects Birkeland currents
- Compared to other parts of the ionospheric current system, the westward electrojet shows little seasonal variation

Correspondence to:
K. M. Laundal,
karl.laundal@ift.uib.no

Citation:
Laundal, K. M., Finlay, C. C., Olsen, N., & Reistad, J. P. (2018). Solar wind and seasonal influence on ionospheric currents from Swarm and CHAMP measurements. *Journal of Geophysical Research: Space Physics, 123*. https://doi.org/10.1029/2018JA025387

Received 23 FEB 2018
Accepted 28 APR 2018
Accepted article online 10 MAY 2018

Abstract We present a new climatological model of the ionospheric current system, determined from magnetic measurements taken by the Challenging Minisatellite Payload (CHAMP) and *Swarm* satellites. The model describes the horizontal currents in the ionosphere, below the satellites, and the field-aligned (Birkeland) currents that connect the ionosphere with the magnetosphere. The model provides ionospheric current values at any location as continuous functions of solar wind speed, interplanetary magnetic field, dipole tilt angle, and the $F_{10.7}$ index of solar flux. Geometric distortions due to variations in the Earth's main magnetic field are taken into account, thus allowing for precise comparisons between the two hemispheres. The model is the first of its kind to describe the full 3-D electric currents and not only the field-aligned or the equivalent horizontal current. We use this capability to demonstrate a key difference between seasons: During winter, the total horizontal current is almost entirely confined to the auroral oval, for all interplanetary magnetic field orientations, where it connects upward and downward Birkeland currents. During more sunlit conditions, the horizontal current extends beyond the auroral oval and is a sum of currents connecting Birkeland currents and currents that circulate in the ionosphere. The westward electrojet is the only large-scale current structure that is persistent across seasons. Comparison with average convection maps suggests that it is comprised largely of Hall currents, which connect to Birkeland currents in the winter but not in summer.

1. Introduction

Geomagnetic disturbances at polar latitudes are associated with highly variable currents in the ionosphere. As discovered by Birkeland (1901), who analyzed magnetic disturbances on ground, the current system is best organized in a reference frame that is fixed with respect to the Sun. We now know this is because the currents are ultimately a result of the interaction between the solar wind and the magnetosphere surrounding the planet. We also know that the current system is three dimensional, flowing horizontally in the lower part of the ionosphere with connections to the outer magnetosphere along magnetic field lines. Field-aligned currents are called Birkeland currents. The existence of Birkeland currents was a source of great controversy for several decades (Egeland & Burke, 2010), despite availability of sophisticated techniques for analyzing ground magnetic field measurements (Chapman & Bartels, 1940), and studies that showed the global morphology of polar magnetic disturbances (e.g., Vestine et al., 1947). The reason for the controversy, as explained by Fukushima (1976), is that measurements of the ground magnetic field perturbations are simply not enough to distinguish between the conflicting current models. Ground magnetic perturbations can be modeled by a purely horizontal current sheet *or* by a three-dimensional current system, involving Birkeland currents.

It was only when magnetic field measurements in space became available, that the existence of Birkeland currents was proven beyond doubt (Zmuda et al., 1966). Iijima and Potemra (1976, 1978) showed that on large scales during active geomagnetic conditions, the Birkeland currents form roughly two concentric rings near the auroral oval. The inner ring is called the Region 1 (R1) current and is the strongest. It is upward at dusk and downward at dawn. The outer ring is called the Region 2 (R2) current, and has the opposite direction of the adjacent R1 current. This large-scale picture has been confirmed and refined in numerous studies since then (B. J. Anderson et al., 2008; Friis-Christensen et al., 1984; Green et al., 2009; He et al., 2012; Juusola et al., 2014; Papitashvili et al., 2002; Weimer, 2001).

It is common to decompose the full three-dimensional ionospheric current system into field-aligned volume current densities, measured in A/m^2, and horizontal height-integrated sheet currents, measured in A/m.

Formally, the horizontal sheet current is defined to be the horizontal part of the vector current density integrated over the height of the ionosphere. This integral will include the horizontal components of the Birkeland currents, but we assume here that these are negligible at polar latitudes, where the field lines are almost vertical. Furthermore, the horizontal sheet current is commonly decomposed in two different ways: (1) Pedersen currents, which flow along the electric field in the neutral wind frame of reference (e.g., Richmond, 1995), and Hall currents, which are perpendicular to this electric field, or (2) a Helmholtz decomposition into 2-D divergence-free and curl-free vector fields. A decomposition into Hall and Pedersen components requires knowledge of the electric field in the neutral wind frame (often assumed to be a purely corotational), while a Helmholtz decomposition can be performed with no additional knowledge. In special cases, the divergence-free and curl-free parts of the sheet current are equal to the Hall and Pedersen currents, respectively, in particular if the magnetic field lines are purely radial, and if horizontal conductivity gradients are either absent or parallel to the electric field (Fukushima, 1976; Vasyliunas, 2007). These assumptions about conductivity are often violated, in which case the relationship between the two decompositions become much more complicated, and the divergence-free and curl-free parts of the current are not perpendicular (see, e.g., Laundal et al., 2015). In this paper, our analysis is primarily based on magnetic field measurements, from which we derive currents. Consequently, we only discuss the separation into Hall and Pedersen components when we have additional information about the electric field.

The decomposition described above, into field-aligned Birkeland currents and divergence-free and curl-free parts of the horizontal sheet current, is useful due to the manner in which the corresponding parts of the magnetic field vary in space. With the approximation that the Earth's main magnetic field, and thereby the Birkeland currents, are purely radial, which is reasonable at polar latitudes, the magnetic field perturbations on ground are only related to the divergence-free part of the horizontal currents and the currents that they induce below ground. The fields related to the curl-free part of the horizontal ionospheric current and the Birkeland currents cancel (Fukushima, 1976; Vasyliunas, 2007). At high altitudes, far above the horizontal current layer, the magnetic field associated with Birkeland currents quickly becomes dominant. The only place where there is a significant magnetic field associated with all parts of the current system is at low Earth orbit. Observations from this region are the focus of this study.

The spatial variation of the ionospheric disturbance magnetic field, described above, has led to the development of a variety of approaches for estimating currents from magnetic field measurements (see review by Vanhamäki & Amm, 2011, and references therein). The equivalent current derived from ground magnetometer data in the polar region, following, for example, Chapman and Bartels (1940), can be treated as synonymous with the divergence-free part of the horizontal current $\mathbf{J}_{df}$, and the full current system can be derived if this is combined with additional information, for example, about the ionospheric conductivity (Friis-Christensen et al., 1984; Kamide et al., 1981). The full current system can also be estimated by combining the equivalent current, derived from ground, with the field-aligned current, derived from magnetometers in space (Green et al., 2007; Laundal et al., 2015). In that case, the curl-free current $\mathbf{J}_{cf}$ is calculated by solving the current continuity equation $\nabla \cdot \mathbf{J}_{cf} = -J_u$, where J_u is the upward current mapped to the height chosen for the equivalent current. $\mathbf{J}_{cf}$ is then added to $\mathbf{J}_{df}$ to give the full sheet current. Both these approaches involve the combination of different data sets and involve assumptions that lead to uncertainties in the estimated horizontal sheet current.

More recently, it has become possible to estimate the full current system from a single set of magnetic field measurements, from low Earth orbit, without a need for additional information. This requires high-precision magnetic field measurements in space, at relatively low altitudes, and an accurate model for subtracting the field from all other sources (core, crust, magnetosphere, etc.). Juusola et al. (2014) demonstrated this, using Challenging Minisatellite Payload (CHAMP) measurements and the spherical elementary current representation of Amm (1997). Laundal, Finlay, et al. (2016) used a different approach, representing the magnetic field and associated currents by a spherical harmonic expansion constrained by measurements from CHAMP and *Swarm*. The spherical harmonic expansion was performed in magnetic apex coordinates (Richmond, 1995), since the current systems and resulting magnetic field disturbances are strongly organized by the Earth's magnetic field. Laundal, Finlay, et al. (2016) showed that consistent use of magnetic apex coordinates, that is, using the apex coordinate frame for describing both location and magnetic field components, resulted in stronger and more confined currents than alternative approaches. Use of magnetic apex coordinates makes the resulting disturbance magnetic field invariant with respect to longitudinal and secular variations of the Earth's magnetic field and allows for precise comparison between hemispheres.

Here we expand on the work by Laundal, Finlay, et al. (2016), and present a general, climatological, global model, based on satellite measurements of the magnetic field, of the complete current system consisting of horizontal sheet currents, and field-aligned currents connecting those with the magnetosphere and outer space. The model is global, and we do not impose any north-south symmetries. The dependence on external parameters is implemented by allowing the spherical harmonic coefficients to vary with the solar wind speed, the interplanetary magnetic field (IMF), the dipole tilt angle, and the $F_{10.7}$ index. This is the first such model to estimate the total horizontal current from a single set of magnetic field measurements without additional assumptions. Previous models either describe only the equivalent current that produces the magnetic disturbance at ground (Weimer, 2013; Weimer et al., 2010), or the Birkeland currents that account for satellite measurements (He et al., 2012; Papitashvili et al., 2002; Weimer, 2001). Taking advantage of this new capability of our model, we investigate how the total polar current system changes with the seasons and the IMF and, in particular, regarding the relationship between horizontal and vertical currents.

The model is distributed to the scientific community under the acronym AMPS (Average Magnetic field and Polar current System) as a Swarm data product, with support from the *Swarm DISC (Data, Innovation, and Science Cluster)*, along with a Python forward code to calculate model magnetic field and current densities (Laundal & Toresen, 2018). The technical details on how the model was derived are presented in section 2 and in Appendix A of this paper. Equations for the global ionospheric currents are given in Appendix B. In section 2.4 we also discuss certain aspects of the interpretation of the model. In section 3 we use the model to investigate how the large-scale current system in the Northern Hemisphere varies in response to changes in dipole tilt angle and IMF orientation. Some of the results from that section are discussed in more detail in section 4. Section 5 concludes the paper.

2. A Model of the AMPS

In this section we describe a new general global model of the full ionospheric disturbance magnetic field and related electric current system, based on magnetic field measurements from low Earth orbit. The model magnetic field is represented by a continuous function in space and time, depending on magnetic latitude, magnetic local time, height, and certain external parameters: the IMF B_y and B_z components, the solar wind speed, the dipole tilt angle, and the $F_{10.7}$ index. The function depends on a set of coefficients that are determined empirically using magnetic field measurements from the CHAMP and Swarm spacecraft. Below, and in Appendix A, we present the details of the model parameterization, the data set and technique used to estimate the model parameters, and certain data misfit statistics. In Appendix B we describe how the associated ionospheric currents can be calculated from the estimated model parameters.

Any magnetic field $\mathbf{B}$ can be expressed as a sum of toroidal and poloidal parts, due to the fact that $\nabla \cdot \mathbf{B} = 0$. In a spherical shell with finite thickness much smaller than its radius, like the shell enclosing the CHAMP and Swarm orbits, the poloidal part can be approximated as the gradient of a scalar V. The sum of the toroidal and poloidal parts of the ionospheric magnetic field $\Delta\mathbf{B}$ can be written as (Backus, 1986; Olsen, 1997)

$$\Delta\mathbf{B} = \Delta\mathbf{B}^{\text{pol}} + \Delta\mathbf{B}^{\text{tor}} = -\nabla V + \mathbf{r} \times \nabla T. \tag{1}$$

We expand the scalar functions T and V in terms of spherical harmonics, using modified apex (MA) coordinates for the toroidal scalar T and quasi-dipole (QD) coordinates for the poloidal scalar V. MA and QD coordinates are variants of magnetic apex coordinates (Richmond, 1995). This approach implicitly takes into account longitudinal, hemispheric, and temporal (secular) variations of the Earth's main magnetic field. We refer to Laundal, Finlay, et al. (2016) for a full discussion, but the main equations from that paper are repeated here, in section A1.

The toroidal magnetic field is associated with radial currents crossing the shell where the satellites fly, in our case the radial component of the Birkeland currents. We use the terms radial/vertical current and Birkeland currents interchangeably, since we focus on polar latitudes where the magnetic field lines are nearly vertical.

The poloidal magnetic field is associated with remote currents that do not enter the shell, in our case the divergence-free part of the horizontal currents below the satellites, which we represent as sheet currents at 110-km altitude. This sheet current density includes contributions from ground-induced currents and the horizontal part of the Birkeland currents, but the dominating contribution is assumed to be ionospheric currents, which are perpendicular to magnetic field lines (the divergence-free part of the sum of Hall and

Pedersen currents). This is also the dominating contribution to the equivalent current derived with ground magnetometers. In this paper, we use the term "divergence-free current" for the divergence-free part of the horizontal ionospheric current derived from space-based observations and "equivalent current" for the horizontal ionospheric current derived from ground magnetic perturbations (which is also necessarily divergence-free, Vasyliunas, 1999). The main difference between the divergence-free current and the equivalent current is the inclusion of ground-induced currents in the divergence-free current, which is often accounted for separately in calculations of the equivalent current. In addition, both quantities correspond to a certain height, the choice of which affects the values of the two current representations differently. We use 110 km in this paper.

In Appendix B we present the equations that relate the magnetic field model parameters to ionospheric currents.

2.1. Generalizing the Spherical Harmonic Analysis of Laundal, Finlay, et al. (2016)

The spherical harmonic analysis presented by Laundal, Finlay, et al. (2016) results in a stationary ionospheric magnetic disturbance field, that represents a time average of the data set used to determine the coefficients in the spherical harmonic expansion. Equations (1) and (A2)–(A7) describe how $\Delta\mathbf{B}$ was related to the spherical harmonic coefficients in the expansions of T and V. In this paper, instead of using constant spherical harmonic coefficients, we allow the coefficients to vary with external conditions, by expanding each coefficient as a function of the external parameters. This approach leads to a single continuous function, relating the magnetic disturbance field at any location to the chosen set of external parameters.

Each spherical harmonic coefficient, for example, g_n^m, is expanded as a function of external parameters, with 19 parameters:

$$\begin{aligned} g_n^m = & g_{n1}^m + g_{n2}^m \sin\theta_c + g_{n3}^m \cos\theta_c + g_{n4}^m \epsilon + g_{n5}^m \epsilon \sin\theta_c + g_{n6}^m \epsilon \cos\theta_c + \\ & g_{n7}^m \beta + g_{n8}^m \beta \sin\theta_c + g_{n9}^m \beta \cos\theta_c + g_{n10}^m \beta\epsilon + g_{n11}^m \beta\epsilon \sin\theta_c + g_{n12}^m \beta\epsilon \cos\theta_c + \\ & g_{n13}^m \tau + g_{n14}^m \tau \sin\theta_c + g_{n15}^m \tau \cos\theta_c + g_{n16}^m \beta\tau + g_{n17}^m \beta\tau \sin\theta_c + g_{n18}^m \beta\tau \cos\theta_c + \\ & g_{n19}^m \mathrm{F}_{10.7}. \end{aligned} \tag{2}$$

The same expansion is used for the other sets of coefficients as well: h_n^m, ψ_n^m, and η_n^m [see equations (A2) and (A3)]. β is the dipole tilt angle (see equation 15 of Laundal & Richmond, 2017, for a definition), in degrees,

$$\theta_c = \arctan2(B_y, B_z) \tag{3}$$

is the IMF clock angle, and

$$\epsilon = 10^{-3} |v_x|^{4/3} \sqrt{B_y^2 + B_z^2}^{2/3} \sin^{8/3}(\theta_c/2) \tag{4}$$

is the Newell et al. (2007) solar wind-magnetosphere coupling function. The solar wind speed in the geocentric solar magnetic (GSM) x direction, v_x, is given in km/s, and the IMF components, B_y and B_z (GSM), are given in nT. The interpretation of ϵ is that it correlates with the rate at which closed magnetic flux is opened through dayside reconnection. We also define a quantity

$$\tau = 10^{-3} |v_x|^{4/3} \sqrt{B_y^2 + B_z^2}^{2/3} \cos^{8/3}(\theta_c/2), \tag{5}$$

which maximizes when the IMF is strictly northward. Repeating the arguments used to justify the interpretation of ϵ (see Newell et al., 2007, section 5), τ is assumed to correlate with the lobe reconnection rate. However, in contrast to dayside subsolar reconnection, lobe reconnection may be asymmetric between hemispheres, and strong evidence exists that it happens preferentially in summer (Crooker & Rich, 1993). This asymmetry is taken into account in our model by the inclusion of cross terms between dipole tilt angle β and τ in equation (2).

Equation (2) is inspired by Weimer (2013), who presents a model of ground magnetic field perturbations parameterized by spherical cap harmonics, with each expansion coefficient depending on B_y, B_z, dipole tilt, solar wind speed, and $F_{10.7}$. He used the IMF magnitude, dipole tilt angle, solar wind speed, and the $F_{10.7}$ index as scale factors for the terms in Fourier series expansions in θ_c. The same approach is used in equation (2),

with two important differences: (1) Instead of using the IMF and solar wind speed directly, we combine them to the coupling functions ϵ and τ, and (2) we include multiplicative cross terms of the scale parameters (except for $F_{10.7}$). The use of cross terms avoids the undesired behavior that any one parameter will completely dominate if sufficiently large; in the model by Weimer (2013), if, say the solar wind speed is very large, any dipole tilt angle effect will, a priori, be negligible. In our model, because of the cross terms, this will only happen if dictated by the data. This should lead to more realistic model values for extreme external conditions. The use of cross terms comes at the expense of more unknowns, which is why we do not extend the Fourier series expansion in θ_c to second order, as Weimer (2013) does. Experiments with alternative expansions show that this choice has little impact on the resulting global current patterns.

The spherical harmonic expansions of V and T (see equations (A2) and (A3)) are truncated at spherical harmonic degrees 45 and 65, respectively, and at spherical harmonic order 3. The total number of model parameters then becomes 14,402. We compared this model to one with spherical harmonic order up to 5, and degree up to 35 and 60. The difference in misfit was very small, despite a total of 19,095 model parameters instead of 14,402. The relatively low truncation level for spherical harmonic order, compared to spherical harmonic degree, implies that the longitudinal resolution of the model is lower than the latitudinal resolution. This choice is due to a similar asymmetry in the structure of the large-scale average ionospheric current pattern, known from previous studies (Weimer, 2001, 2013).

2.2. Data

The model parameters are determined empirically, using magnetic field vector measurements from CHAMP (Reigber et al., 2002), from August 2000 to September 2010, and Swarm (Friis-Christensen et al., 2006), from December 2013 to August 2016. CHAMP was launched on 15 July 2000, to a nearly circular orbit of 450 km altitude and 87.3° inclination. It remained in orbit for more than 10 years, providing measurements from altitudes down to 250 km before it decayed in September 2010. Among its payload were a scalar magnetometer and two fluxgate magnetometers measuring the vector magnetic field. The magnetometers were mounted on a 4-m-long boom, with the fluxgates placed on an optical bench along with star cameras to accurately determine the instrument orientation. A similar but improved concept for magnetic field measurements was adopted for the Swarm satellite trio. Swarm was launched in November 2013, from Plesetsk in Russia, the same launch site as CHAMP. Swarm Alpha and Charlie were maneuvered to ≈460 km altitude with an orbital inclination of 87.4°. Swarm Bravo was placed at ≈530 km altitude with 88° inclination. Initially, all three satellites were in nearly the same orbital plane, but due to the different orbital elements the plane of Bravo slowly rotates with respect to the plane of Alpha and Charlie, which remain side by side. Bravo thus provides simultaneous information from a different local time compared to Alpha and Charlie. A long mission is currently foreseen.

We use 1 Hz magnetic field measurements, downsampled every 30 s (discarding 29 out of 30 measurements). For each measurement we subtract magnetic field predictions of the core, lithospheric, and large-scale magnetospheric field as given by the CHAOS-6 model (Finlay et al., 2016). Since our new model is in principle valid at all times, the only selection criterion is that simultaneous solar wind data are available. The solar wind data that we use are time shifted to the bow shock nose, at 1-min time resolution (King & Papitashvili, 2005), and then averaged over the previous 20 min. This choice is discussed in more detail in section 2.4.1.

In total, we have 16,839,394 magnetic vector triplets from which we estimate the 14,402 model parameters using an iteratively reweighted least squares approach using Huber weights (Huber, 1964). In each step, each equation is reweighted according to how well the corresponding data point fits the model prediction from the previous iteration. The purpose of this procedure, which is described in detail in section A2, is to reduce the effect of outliers, and to enable the final solution to better represent typical values rather than simple mean values. Measurements from the Swarm Alpha and Charlie satellites are weighted by 0.5. The reason for this is that they fly side by side and do not provide independent information on the scales resolved by our model.

Figure 1 shows the distributions of external parameters and spatial coordinates for the measurements used to estimate the model parameters. These distributions show which conditions, and which regions, have been used to constrain the solution. In principle, this also indicates the conditions for which the model is most reliable. For example, it is reasonable to expect that the model is better at representing periods when the IMF is 3 nT rather than 12 nT, considering the distribution in the top left panel of Figure 1. However, in addition to the colored histograms, black curves outline the weighted distribution, using the Huber weights of the last model iteration. If the model representation was flawed for more extreme conditions, the Huber weighted

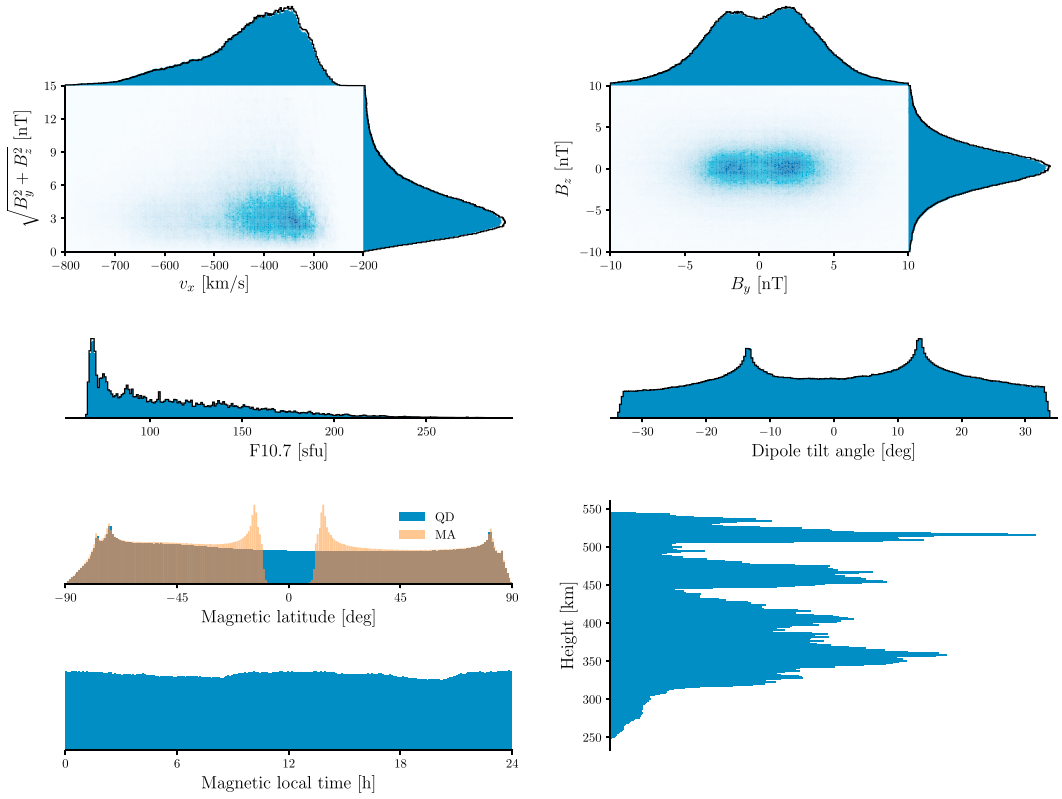

Figure 1. Histograms showing how the data points used to make the model are distributed with respect to different variables and coordinates, denoted by axis labels. Each histogram is based on 16,839,394 points, except for the solar wind plots which are truncated at the extreme ends of the distributions. Measurements from Swarm Alpha and Charlie are weighted by 0.5 in these plots. In the 2-D plots, increasingly dark blue color denotes more frequent values.

distributions would be expected to more strongly peak at the most frequent conditions and go to zero at the ends where the data fit would be poor. This is not the case, which indicates that the model generally represents well the ionospheric magnetic field and associated currents.

The distributions of magnetic latitudes in Figure 1 show that there are no measurements at the modified apex equator (recall we use a reference height of 110 km). Thus, the variation of the toroidal scalar T at low latitudes is not constrained by data. Consequently, the currents associated with T, the vertical currents, are only meaningful poleward of approximately ±45°. V, on the other hand, is well defined at low latitudes, since it is expressed in QD coordinates. The associated current is an estimate of the equatorial electrojet and Sq current systems. The equatorial data gap in MA coordinates, which is not present in QD coordinates, is probably the reason why we need to apply some regularization when inverting for the coefficients relating to T, but not when inverting for the coefficients relating to V. The applied model regularization is described in detail in section A2.

2.3. Misfit and Validation

Figure 2 shows how well the model fits the data at different latitudes, taking into account the Huber weights of the final iteration. The two curves represent the weighted root-mean-squares (RMS) of the measured magnetic field components (denoted **d**) and of the residuals after subtracting model values, **e**, as functions of QD latitude. A perfect model, that captures all variations that are not present in the CHAOS-6 magnetic field model, would give zero RMS of **e**.

The RMS of **e** is less than the RMS of **d** at all latitudes, but the relative difference is largest near the poles. We also see that the shapes of the two curves are different, with the peaks of the RMS **e** equatorward of the peaks of the RMS **d**. Our interpretation of this is that the model does well at representing magnetic disturbances at the most common locations of the auroral oval, but becomes less precise when the auroral oval expands very far equatorward. The thin lines show the RMS of **d** and **e** at conjugate latitudes, in order to ease

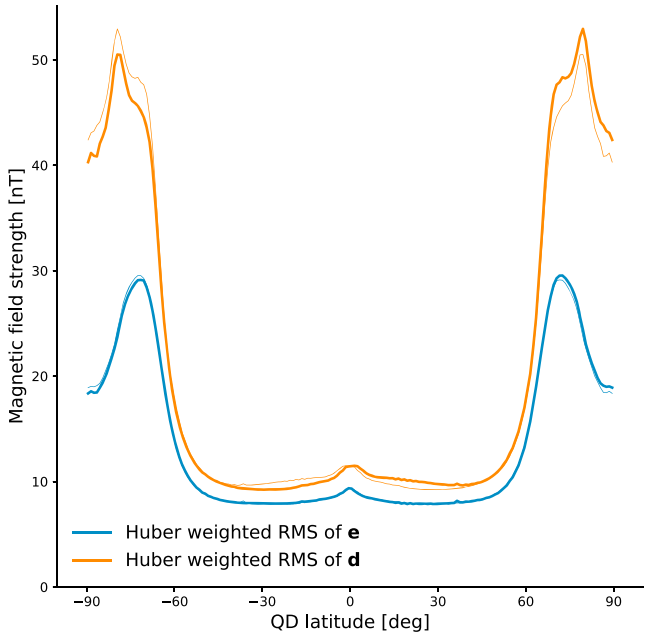

Figure 2. Latitudinal distribution of the weighted root-mean-square of the magnetic field vector components used to make the model (**d**), and the residuals, model minus data (**e**). The thin lines show the same quantities only in the reverse direction, in order to ease comparison between hemispheres. The weights are the Huber weights in the last iteration and the 0.5 fixed weight for the two adjacent Swarm satellites.

comparison between hemispheres. It is interesting to note that the north-south asymmetry in the data **d**, with stronger average magnetic fields in the north, is not present in the data residuals **e**. Presumably, this is due to geometric differences in the Earth's magnetic field, whose effects are accounted for by our model.

In Figure 3 we compare model predictions to independent magnetic field measurements taken by the Ørsted satellite, between March 1999 and July 2000. Ørsted measurements were not used for determining the model, and all the measurements were obtained prior to the first data point from CHAMP. The preprocessing and data selection was similar to the data used in estimating the model: We sample every 30 s, and subtract the CHAOS-6 model predictions (Finlay et al., 2016). The top panel shows the latitudinal variation in the RMS of (1) the Ørsted magnetic field components after subtraction of CHAOS-6 model predictions of the core, lithospheric, and magnetospheric fields, and (2) the residuals when further subtracting the predictions of our model (AMPS). The difference is indicated by color. For both curves, the robust mean, using Huber weights, was used when calculating the RMS. Large differences imply that the model includes more of the absolute variation of the measured magnetic field. The bottom panel shows the prediction efficiency (Detman & Vassiliadis, 1997), $1 - \mathrm{var}(\mathbf{e})/\mathrm{var}(\mathbf{d})$, where **d** and **e** are sets of data and residuals, respectively, and var denotes the variance, calculated robustly, with Huber weights. A value of 1 indicates perfect prediction, and a value of 0 is what we would get by predicting a constant value equal to the mean of **d**. Negative values mean that the prediction does more harm than good.

We see that the model performance is best close to the magnetic poles, where the residual magnetic field is strongest. At middle and low latitudes, the prediction efficiency remains positive, with some notable exceptions. We believe that this is partly related to how the ionospheric currents are related to sunlight and to the main magnetic field at high and low latitudes: The use of magnetic apex coordinates is beneficial when describing currents that are mainly organized by the main field, which is the case at high latitudes. The set of model variables λ (magnetic latitude), ϕ_{mlt} (magnetic local time) and β (dipole tilt angle) describe quite precisely how the outer part of the magnetic field line crossing a certain point is oriented with respect to the Sun. This is important for describing the solar wind-magnetosphere interaction, which is of fundamental importance for high-latitude currents. The same three variables only approximately describe the insolation at that point, however, which would be better described in geographic coordinates. This becomes critical at lower latitudes, where the currents are primarily controlled by sunlight instead of the solar wind-magnetosphere coupling. Especially in the Southern Hemisphere, the longitudinal variations in the main magnetic field are

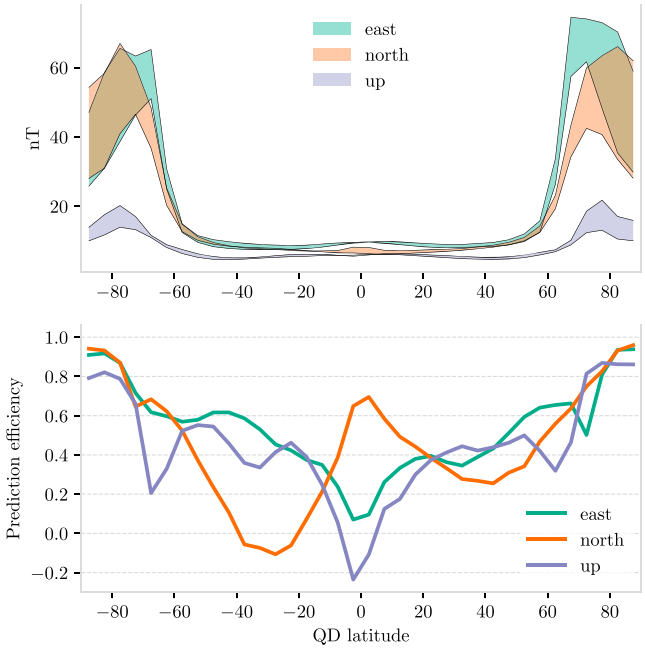

Figure 3. (top) Latitudinal variation in the root-mean-square of Ørsted magnetic field measurements (with main field model subtracted), and the same measurements with model values subtracted. The colored regions indicate the difference. The calculations are done in 5° bins in quasi-dipole latitude and are based on data from March 1999 to July 2000. (bottom) The prediction efficiency of the model when estimating the magnetic field at the times and locations of the Ørsted measurements.

large, which may explain why the prediction efficiency for the northward component becomes negative at $\approx -30°$ QD latitude. At the QD equator, the location for the equatorial electrojet, the upward component becomes very weak (≈5 nT), which probably explains why the prediction efficiency reaches a sharp minimum there.

The remaining residuals at polar latitudes are probably caused by the highly variable, small-scale features of the magnetic perturbations at low Earth orbit, which are not captured by our global model. We will show in section 3 that the model reproduces known variations in the large-scale Birkeland currents with IMF and seasons.

2.4. Interpretation of the Model

The actual current system is arguably never static, always more fine scaled than the model representation, and influenced by processes that are not well represented by the model parameterization. Therefore, the real currents will never be exactly like the model currents. The model currents essentially represent the large-scale average effects of the processes influenced by the parameters that are included in the model: the solar wind speed, the IMF in the *yz* plane, the dipole tilt angle, and the $F_{10.7}$ solar flux index. It should be regarded as an equation of state, corresponding to a quasi-static description of current system and magnetic field, rather than a dynamic description.

Nightside reconnection is not parameterized in the model, despite it being as important for ionospheric electrodynamics as dayside reconnection (e.g., Milan et al., 2017). The main reason for this is that there is presently no reliable proxy for nightside reconnection, which is as accessible and well tested as the solar wind-based proxies for dayside reconnection. An average effect of nightside reconnection is of course present in the model currents, although it is likely reduced by the iterative fitting process and model formulation. Variations in the measured magnetic field that are due to nightside dynamics, and uncorrelated with any of the external parameters of the model, will be poorly fitted and receive low Huber weights in the model estimation procedure.

Waters et al. (2015) adopt an alternative approach for generating global maps of ground magnetic field perturbations in the northern hemisphere, in which the global maps are functions of sunlight (solar irradiance) and a selection of geomagnetic indices, while the solar wind conditions are completely omitted. That approach

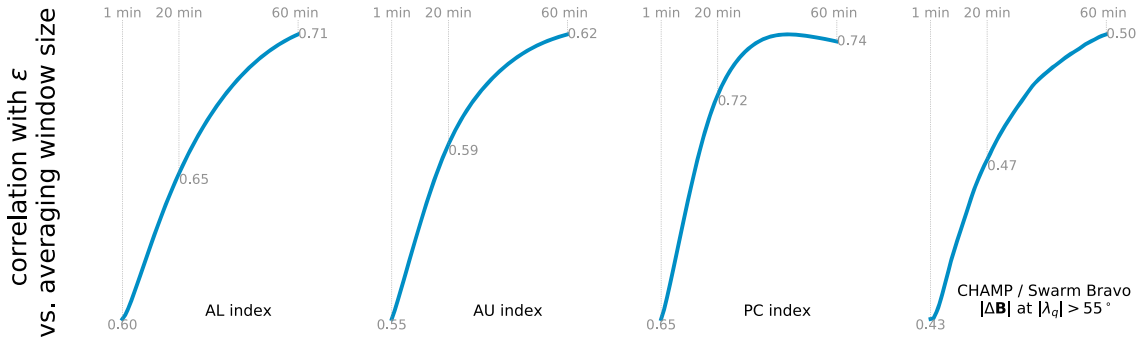

Figure 4. Plots of the Pearson correlation coefficient of four different geomagnetic parameters, at 1-min time resolution, with the Newell et al. (2007) ϵ [equation (4)] coupling function as a function of averaging window size for ϵ. The temporal averaging is applied only to ϵ. Correlation coefficients at three different averaging window sizes are indicated in each plot. The indices and solar wind data come from the OMNI database. The $\|\Delta\mathbf{B}\|$ values used in the right plot are from CHAMP/Swarm Bravo 1-Hz data, downsampled at 1-min cadence, in the region poleward of 55°. The plot is based on the period 2000–2016.

may give a better fit to the data, but it is more difficult to interpret in terms of cause and effects. In contrast, our model can be used to test ideas concerning solar wind/magnetosphere/ionosphere coupling processes. For example, in section 3 we present maps of the current system for certain IMF orientations and tilt angles, which can be used to separately assess the average seasonal or IMF effects, by keeping other parameters fixed.

2.4.1. Choice of Temporal Averaging

Our model is parameterized by 1-min solar wind data time shifted to the bow shock, and then averaged over the previous 20 min. The motivation behind this choice is that we want the input to represent, at least on average, the instantaneous solar wind that affects the magnetopause. Naively, this suggests using as high time resolution input as possible. However, we believe it is better to apply some time averaging because (1) even for the direct solar wind influence, it takes about 10–20 min before the global current patterns adapt to changes (Snekvik et al., 2017), (2) in situ high-resolution measurements of the solar wind may not be a good representation of its large-scale structure due to spatial variations/turbulence, and (3) the time shift from the solar wind monitor to the magnetopause will be imperfect.

In Figure 4 we show the correlation between high time resolution geomagnetic indices and the ϵ parameter averaged over increasingly large windows, ranging from 1 to 60 min. The correlation increases monotonically in all cases, except for the case of the PC (polar cap) index. This increase is attributed in part to the effects described in the previous paragraph. However, another effect probably takes over at some point: On long time scales, the dayside reconnection (which is believed to be proportional to ϵ) equals the nightside reconnection, so that the time average of ϵ becomes a good representation of both the directly driven component and the so-called unloading component of the solar wind-magnetosphere system. On short time scales, dayside and nightside reconnection seem to be much less correlated (Hubert et al., 2006). We interpret the initial increase in correlation coefficients in Figure 4 as an effect of time delays related to the directly driven component, and the less rapid continuing increase, after $\approx$ 20 min, as an effect of nightside processes. Since our aim is to model the average effects associated with the directly driven component, we choose an averaging window of 20 min. Figure 4 suggests that a better fit could be achieved by choosing an averaging window >60 min. However, considering the different processes involved, this would make the interpretation of the model more ambiguous.

3. Results

In this section we present climatological maps of the large-scale current systems in the Northern Hemisphere, for various tilt angles and IMF orientations. One reason for presenting these maps is to check whether our model is able to reproduce well-known features found in previous studies (section 3.1). Since our model also includes a new and more direct way of estimating the total current system, we additionally present the dependence of the average horizontal sheet current density on seasons and IMF in section 3.2. In section 4, we discuss the relationship between field-aligned and horizontal currents, and how this changes with seasons.

Figures 5–7 show the vertical currents and the divergence-free part of the horizontal current sheet densities, with the dipole tilt angle set to −25° (corresponding to Northern winter), 0° (equinox), and +25° (Northern summer), respectively. In Figures 9–11 these currents are combined to show similar plots of the

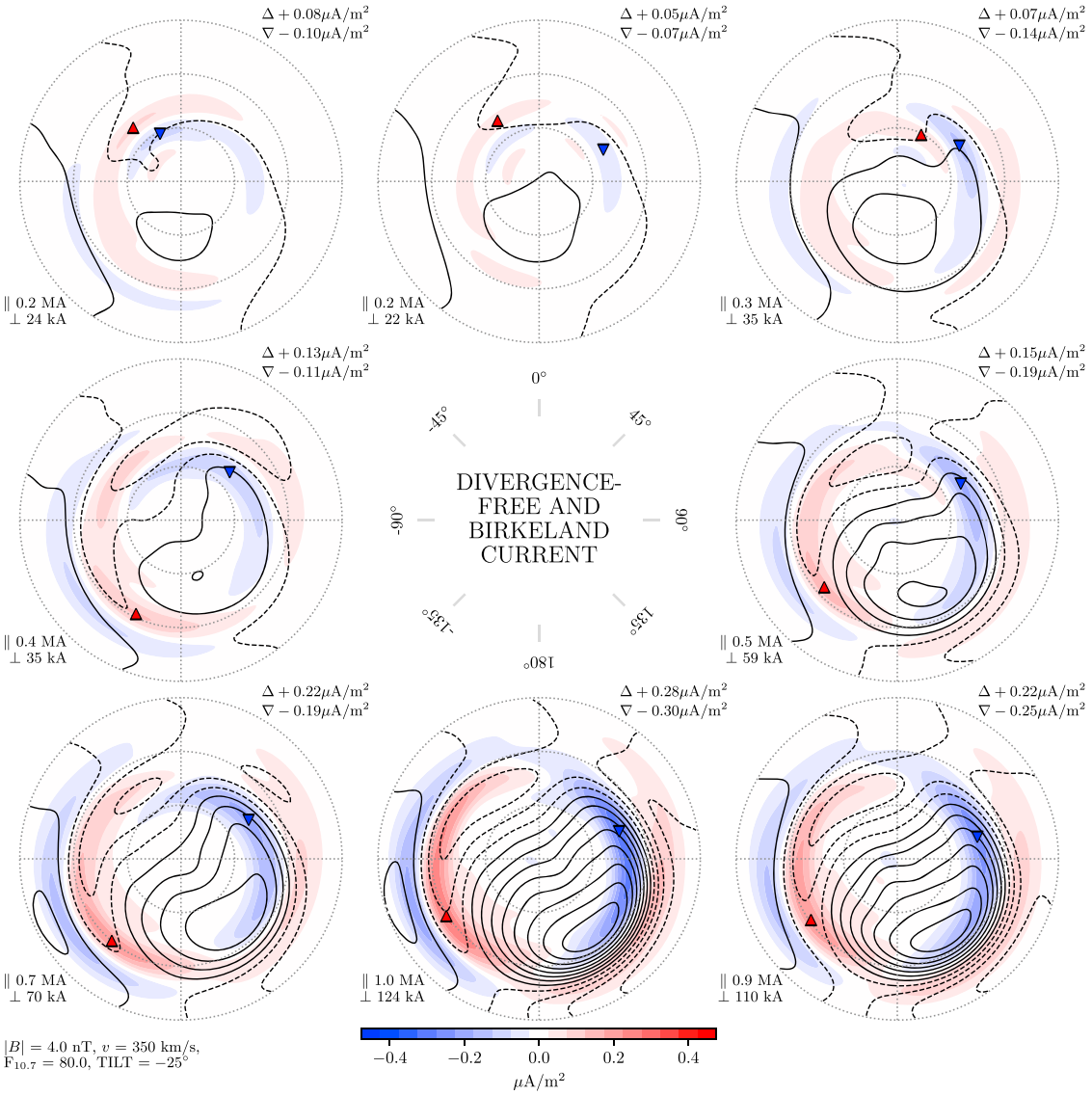

Figure 5. Field-aligned current (red and blue color) and the divergence-free current function (black contours), in the Northern Hemisphere, shown for eight different interplanetary magnetic field clock angle orientations indicated at the center. Each map shows the apex north pole at the center, with latitude circles indicated at 80°, 70°, and 60°. Magnetic noon is up, midnight down, dawn to the right, and dusk to the left. The external conditions used for this plot are indicated in the lower left corner. Notice that the dipole tilt angle for this plot is −25° (Northern *winter*). The peak upward and downward current densities are listed in the top right corners, and the peak locations indicated by red and blue triangles. The scale of the field-aligned current densities is given at the bottom. The total upward current poleward of 60° magnetic latitude is given in the lower left corners, labeled by ∥, in units of megaampere. The number labeled by ⊥ is a measure of the total divergence-free current, namely, the difference between the maximum and the minimum of the divergence-free current function Ψ, in units of kiloampere. Ten kiloamperes flow between each black contour of Ψ. Negative values of Ψ are indicated by dashed contours and positive values by solid contours. The purpose of this distinction is to show the direction of the gradient of Ψ, since any constant can be added to Ψ, changing the zero level, without changing the currents. Current direction is clockwise around maxima of Ψ and counterclockwise around minima.

true horizontal current sheet densities, which are not divergence-free since they are in part fed by Birkeland currents. The details of how the true horizontal current is calculated are given in section 3.2 and in Appendix B. In each figure, the IMF magnitude is 4 nT, the solar wind speed is set to 350 km/s, and $F_{10.7}$ to 80 sfu. These parameters are close to the peaks of the distributions in Figure 1. The IMF clock angle is indicated at the center of each figure.

All presented results are based on model currents from the Northern Hemisphere. The model also includes currents and magnetic fields in the Southern Hemisphere. The results obtained below are also largely valid in the Southern Hemisphere, if we reverse the signs of the dipole tilt angle and the IMF B_y. However, this

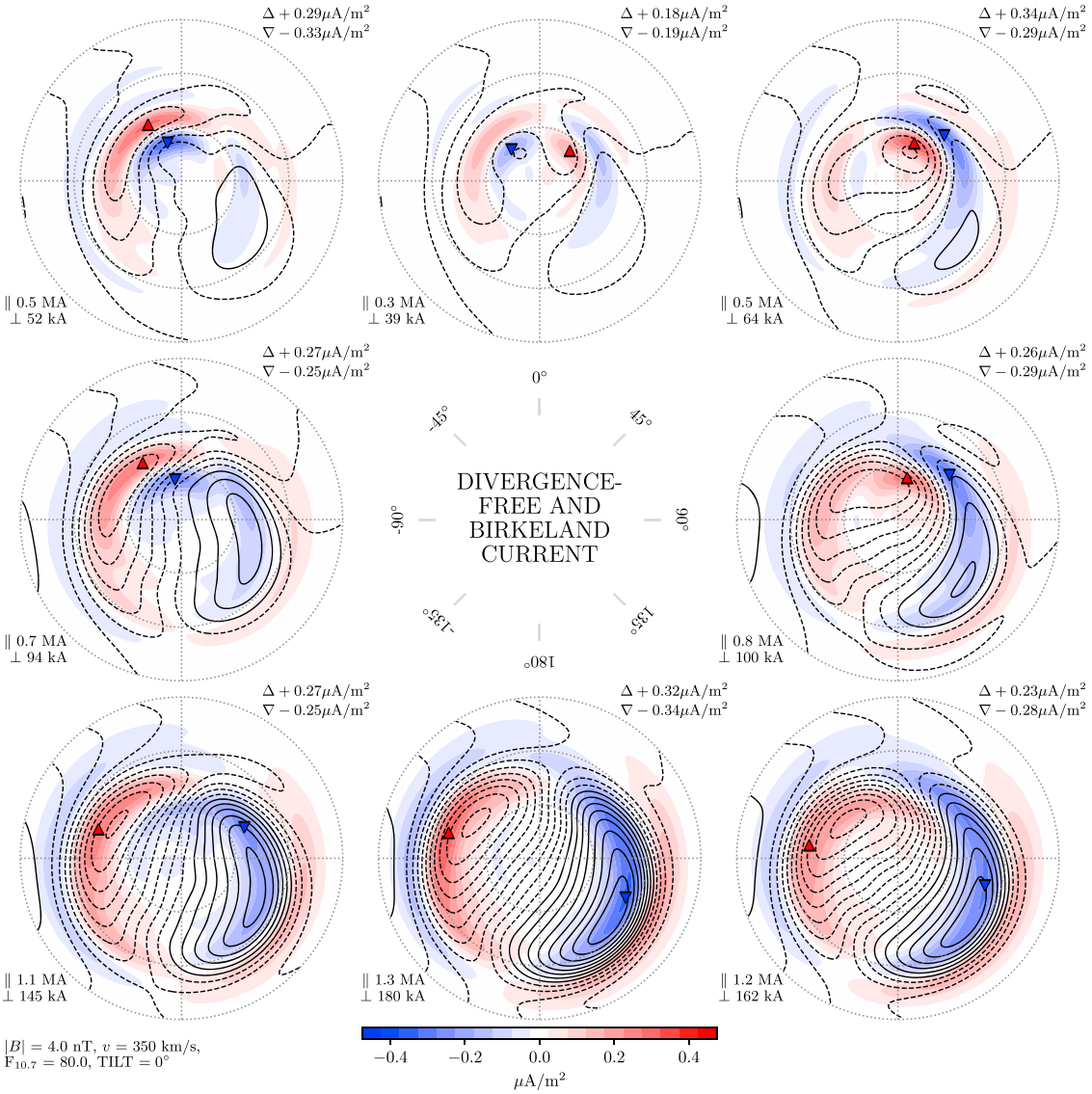

Figure 6. Same as Figure 5, only with tilt angle 0° (*equinox*).

hemispheric symmetry is only approximate, since no symmetries are imposed in the model. Detailed investigations of the differences will be the topic of future studies.

3.1. Comparison to Previous Studies

Figures 5–7 show maps of Birkeland current densities and of the divergence-free part of the horizontal sheet current density. There have been several studies that show similar maps of Birkeland currents, and below we compare those maps to the currents presented here. We also compare the divergence-free part of the horizontal current, shown as contours in Figures 5–7, with previous studies of equivalent currents derived from ground magnetometers. To our knowledge, there are no similar studies of these currents derived from space.

3.1.1. Comparison With Birkeland Currents

The global average configuration of Birkeland current densities was first reported in the iconic studies by Iijima and Potemra (1976, 1978). The currents that they termed R1 and R2 are seen in all the maps in Figures 5–7, but most strongly for southward IMF. They also noticed that R1 tends to be stronger than R2, which our model confirms. Iijima and Potemra based their findings on magnetic observations from the Triad satellite. Since then, global maps of Birkeland currents have been derived using magnetometer measurements from Dynamics Explorer 2 (Weimer, 2001), Ørsted and Magsat (Papitashvili et al., 2002), the fleet of Iridium satellites

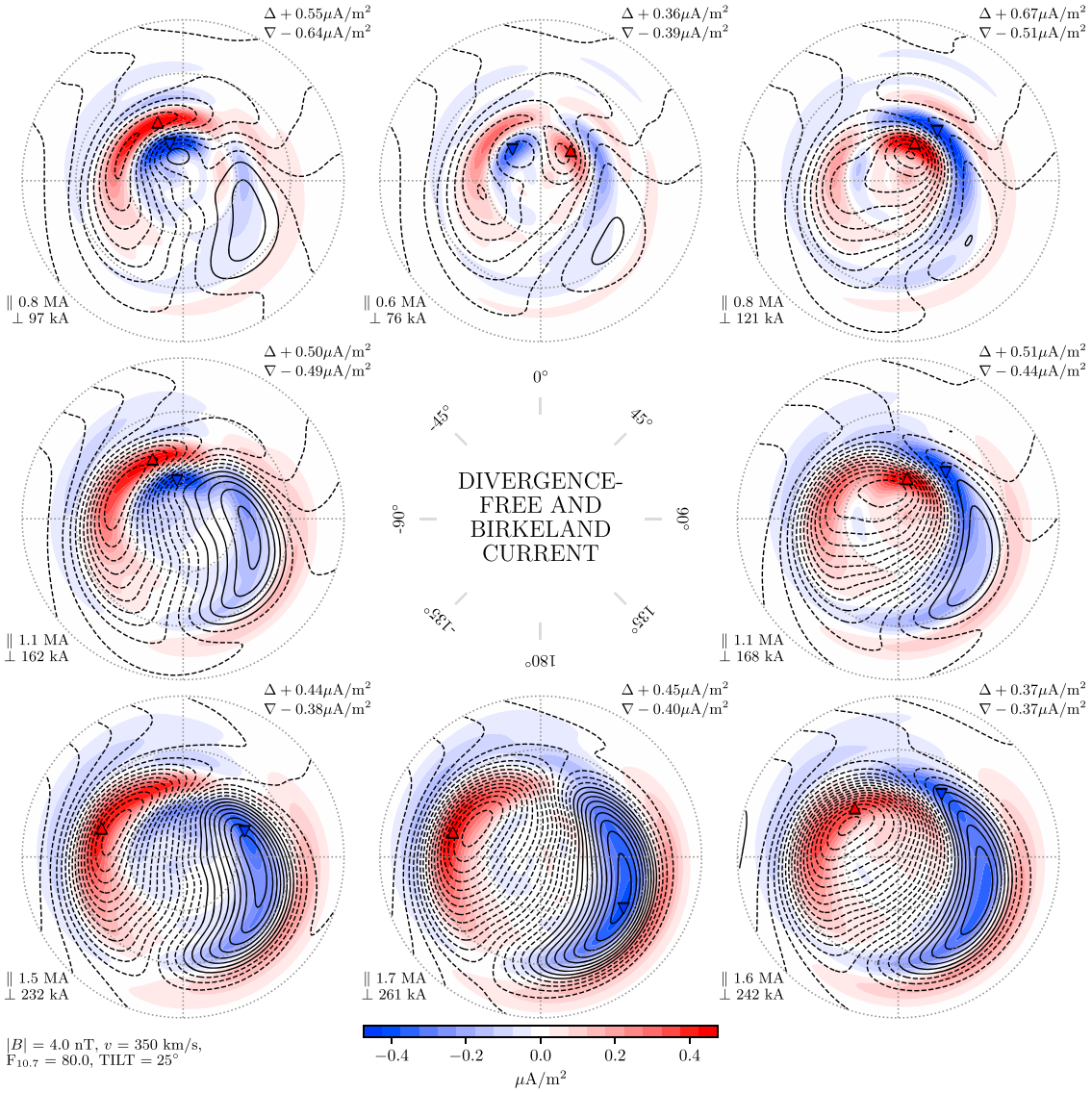

Figure 7. Same as Figure 5, only with tilt angle 25° (*summer*).

(B. J. Anderson et al., 2008; Green et al., 2009), and CHAMP (Juusola et al., 2014). Magnetic field measurements from ground have also been used, together with a model of ionospheric conductance, to estimate Birkeland currents (Friis-Christensen et al., 1984). Since 2010, polar maps of Birkeland currents have been available at 10-min time resolution, from the Active Magnetosphere and Planetary Electrodynamics Response Experiment (AMPERE; B. J. Anderson et al., 2000; Waters et al., 2001), based on magnetic field measurements from the Iridium satellites. The following discussion is primarily based on comparison with the study of Green et al. (2009), who found that their current patterns were in general agreement with previous results. It is also convenient, since they present their current patterns in a similar format as we do.

The main features of the Birkeland current patterns identified in the mentioned studies are confirmed by our model: on the dayside, the currents are very sensitive to the sign of the IMF B_y component, with upward current around noon poleward of a downward current when $B_y > 0$ and the opposite when $B_y < 0$. These dayside currents are strongly dependent on the season, with much stronger currents in the summer. The dayside B_y-dependent currents appear during both signs of B_z, but they are weaker and farther from the pole when it is negative. On the nightside, the B_y variations are much less pronounced. The seasonal variations are also less severe on the nightside than on the dayside. However, our model confirms previous reports that the currents in the premidnight sector are strongest in winter (darkness; Ohtani et al., 2005).

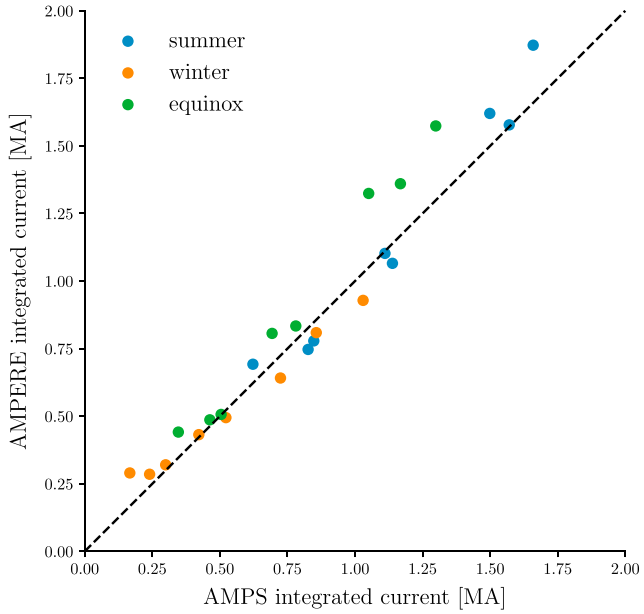

Figure 8. The integrated upward current from the maps in Figures 5–7 compared to average integrated currents from AMPERE during similar conditions. The dashed line shows where the two currents are equal. The points are color coded by season. The AMPERE currents are averages in bins defined by IMF $B = 4 \pm 1.5$ nT; $v = 350 \pm 50$ km/s; tilt angle either $< -20°$, $0 \pm 10°$, or $>20°$; and clock angle in 45° wide bins centered at the eight clock angles used in the maps in Figures 5–7. When integrating AMPERE maps, current densities <0.2 μA are considered to be noise and neglected, following Coxon et al. (2016). We used AMPERE data from January 2010 to December 2016, and each bin includes at least 2,856 maps. AMPERE = Active Magnetosphere and Planetary Electrodynamics Response Experiment.

The opposite seasonal variations on the dayside and nightside lead to a clear shift in the peak upward current, from the dayside in the summer to the nightside in winter. During northward IMF, however, the model nightside currents are almost absent, and the peak remains on the dayside, independent of the season. Similar seasonal variations are not seen in the downward dawn R1 current.

Some of the features observed in Figures 5–7 are different from the currents reported by Green et al. (2009). The strongest current densities in the study by Green et al. (2009) appear near dawn and dusk, in summer, during southward IMF. In our model, the strongest current densities also occur in summer, but they are associated with northward IMF. In the maps in the top corners of Figure 7, the peak currents are ≈50% stronger than the peak current in the map representing strictly southward IMF. These dayside currents are of course much more confined than the R1 currents during southward IMF, so the integrated currents are smaller.

There are also subtle differences in the overall current configuration. Our currents are more poleward located, and the current sheets are narrower than those presented by Green et al. (2009). The former point can probably be explained by the difference in data selection; Green et al. (2009) based their figures on more active periods, when the auroral oval is expected to be larger, whereas our model is based on all geomagnetic conditions, including quiet periods. The latter is likely an effect of different representations and inversion techniques. In particular, the stronger, more confined high-latitude dayside currents in our model, compared to the average current maps reported by Green et al. (2009), are probably due to the use of apex coordinates, instead of geomagnetic dipole coordinates. We also note that our current maps show stronger R2 currents. Green et al. (2009) noted that their R2 currents may be too weak, due to the relatively poor sensitivity of the magnetometers on board the Iridium satellites.

The integrated upward current is shown in the lower left corner of each map, labeled by ||. Since the model is global, there is no guarantee that the upward current is balanced by the downward current in the same hemisphere. Nevertheless, this turns out to be the case to a good approximation, which means, as expected, that there is little leakage of Birkeland current to lower latitudes. In Figure 8 we compare the integrated currents from each of the 24 maps in Figures 5–7 to average total currents in AMPERE maps during similar conditions. We see that the current values are very similar with the two approaches. We note however that this

comparison only addresses the Northern Hemisphere, which on average has stronger AMPERE-derived currents than the South, according to Coxon et al. (2016). A detailed investigation of north-south asymmetries in our model will be presented in a future paper.

3.1.2. Comparison With Equivalent Currents

The contours in Figures 5–7 represent the scalar current function Ψ, defined in equation (B3), which relates to the divergence-free part of the horizontal currents flowing below the satellites. A fixed amount of current, 10 kA, flows between each contour. The current direction is parallel to the contours. The equatorward portion of the dawn cell is the westward electrojet. Presumably, this current will be very similar to the equivalent current observed from ground, which corresponds to the divergence-free part of the horizontal current in the ionosphere (e.g., Laundal et al., 2015; Vasyliunas, 2007). The main concern with this comparison is that the divergence-free horizontal current in Figures 5–7 contain contributions from ground-induced currents (since the ionospheric and the Earth-induced currents are internal to the satellite orbits and hence cannot be separated), while such currents are often accounted for in calculations of the equivalent current from ground-based magnetometers. Nevertheless, Laundal, Finlay, et al. (2016) showed that the two current functions have very similar morphologies, and so we devote this section to compare the divergence-free currents from our model with previous studies based on ground magnetometers. We are not aware of any similar studies that use space-based magnetometers to estimate this current for different IMF orientations and seasons.

Polar equivalent currents have been reported in the scientific literature for more than a century (Birkeland, 1901), but relatively few studies investigate their global variation with seasons and IMF. In a pioneering study based on a chain of Greenland magnetometers, Friis-Christensen and Wilhjelm (1975) showed that equivalent currents have a very different variation with B_y in summer and winter. In summer, the equivalent currents behave much like the polar region plasma convection, only in the reverse direction. This implies that it is a Hall current. In winter, however, the equivalent current pattern deviates from the average convection, which means that it is not only a Hall current. This observation was confirmed in a large statistical study based on SuperMAG magnetometers (Laundal, Gjerloev, et al., 2016). It is an effect of the conductivity being greatly reduced in the polar cap when it is dark, so that distant effects of Birkeland currents dominate the magnetic field signal on ground (Laundal et al., 2015). This is discussed in more detail in section 4.2.

We compare Figure 6 in Laundal, Gjerloev, et al., (2016) to the bottom rows of Figures 5–7. Like the equivalent current, the divergence-free current in Figures 5–7 has a clear seasonal variation, resembling convection patterns (e.g., Haaland et al., 2007; Pettigrew et al., 2010) in summer, but not in winter. In winter, during southward IMF, a dawn cell dominates completely. The magnitude of this cell is much stronger when B_y is positive than when it is negative. During summer, the dawn cell displays an opposite, but significantly weaker, asymmetry with respect to B_y. This is in good agreement with the equivalent current observations by Laundal, Gjerloev, et al. (2016). A similar variation with seasons and B_y is observed in the *AL* index (Friis-Christensen et al., 2017), which represents the strength of the westward electrojet.

The total current flowing between the maximum and minimum of the current function is indicated in the lower left corner of each map in Figures 5–7, next to $\perp$, in units of kiloampere. We see that there is a strong asymmetry in magnitude with respect to B_y in the winter, with much stronger currents when B_y is positive than when it is negative. The same asymmetry was found in the equivalent current patterns derived from ground, by Laundal, Gjerloev, et al. (2016). Based on all the nine cases with B_z negative, we find that the current magnitudes in these two studies are correlated with a Pearson correlation of 0.97. The scales are different, however, with the current in Figures 5–7 only $\approx$60% of the current detected from ground. The main reason for this is probably that the binned average currents of Laundal, Gjerloev, et al. (2016) corresponded to stronger solar wind driving than the currents in Figures 5–7. Other possible reasons include the influence of ground-induced currents and differences in inversion techniques.

The generally good agreement between the divergence-free part of the horizontal currents derived from space and the equivalent current from ground suggests that the effect of ground-induced currents on the model divergence-free currents is modest. The similarities encourage another application for the model, to be explored in future studies: If the divergence-free current function can be treated as a good approximation

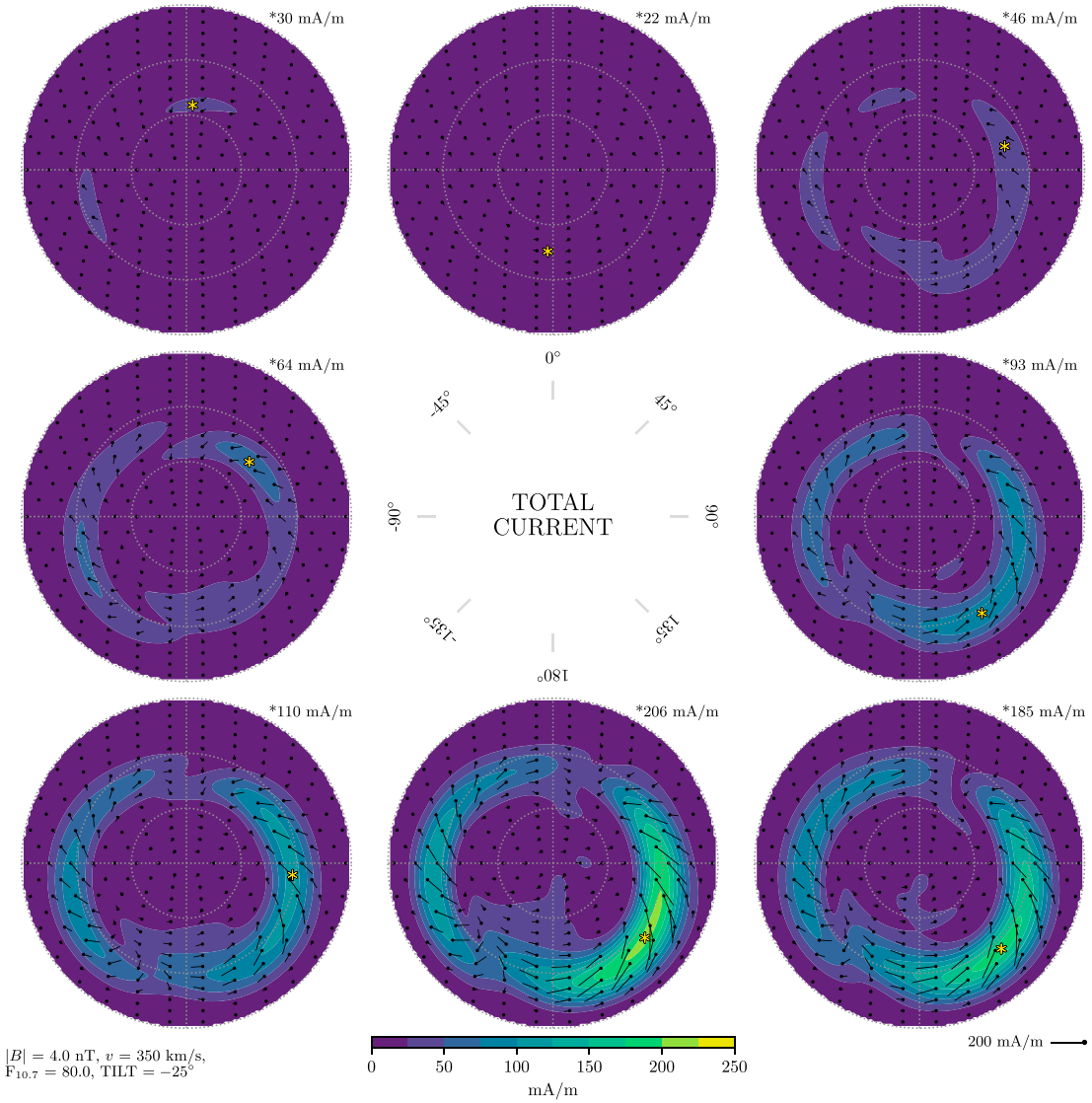

Figure 9. Total horizontal sheet current densities in the Northern Hemisphere during *winter*, calculated by combining the currents of Figure 5. The vectors show the direction and magnitude of the current, with the scale indicated in the lower right corner. The background color also indicates the current magnitudes. The peak current is indicated at the top right corners of each map, and its location by a yellow asterisk. The format is otherwise the same as in Figure 5.

to the ground-based equivalent current function, the associated magnetic field perturbations on ground can be easily calculated. In future versions of the model, this link can also be used to include ground magnetometer measurements in the inversion.

3.2. The Total Horizontal Current

The previous section dealt with Birkeland currents and the divergence-free part of the horizontal current sheet density. According to the Helmholtz theorem these can be combined to calculate the total horizontal current sheet density, **J**. The divergence-free part, $\mathbf{J}_{df} = \mathbf{k} \times \nabla\Psi$, where Ψ is the divergence-free current function [equation (B3)], shown with black contours in Figures 5–7, and **k** is an upward unit vector. The curl-free part, $\mathbf{J}_{cf} = \nabla\alpha$, is calculated from the current continuity equation, $\nabla \cdot \mathbf{J}_{cf} = \nabla^2\alpha = -J_u$, where J_u is the upward current density shown in color in Figures 5–7. The solution, and the full expressions for the horizontal current components in terms of model coefficients, are given in Appendix B. It is a unique property of our model that **J** can be estimated directly from the same set of magnetic field measurements, without the need for any assumptions about ionospheric conductivity or plasma convection (i.e., the ionospheric electric field).

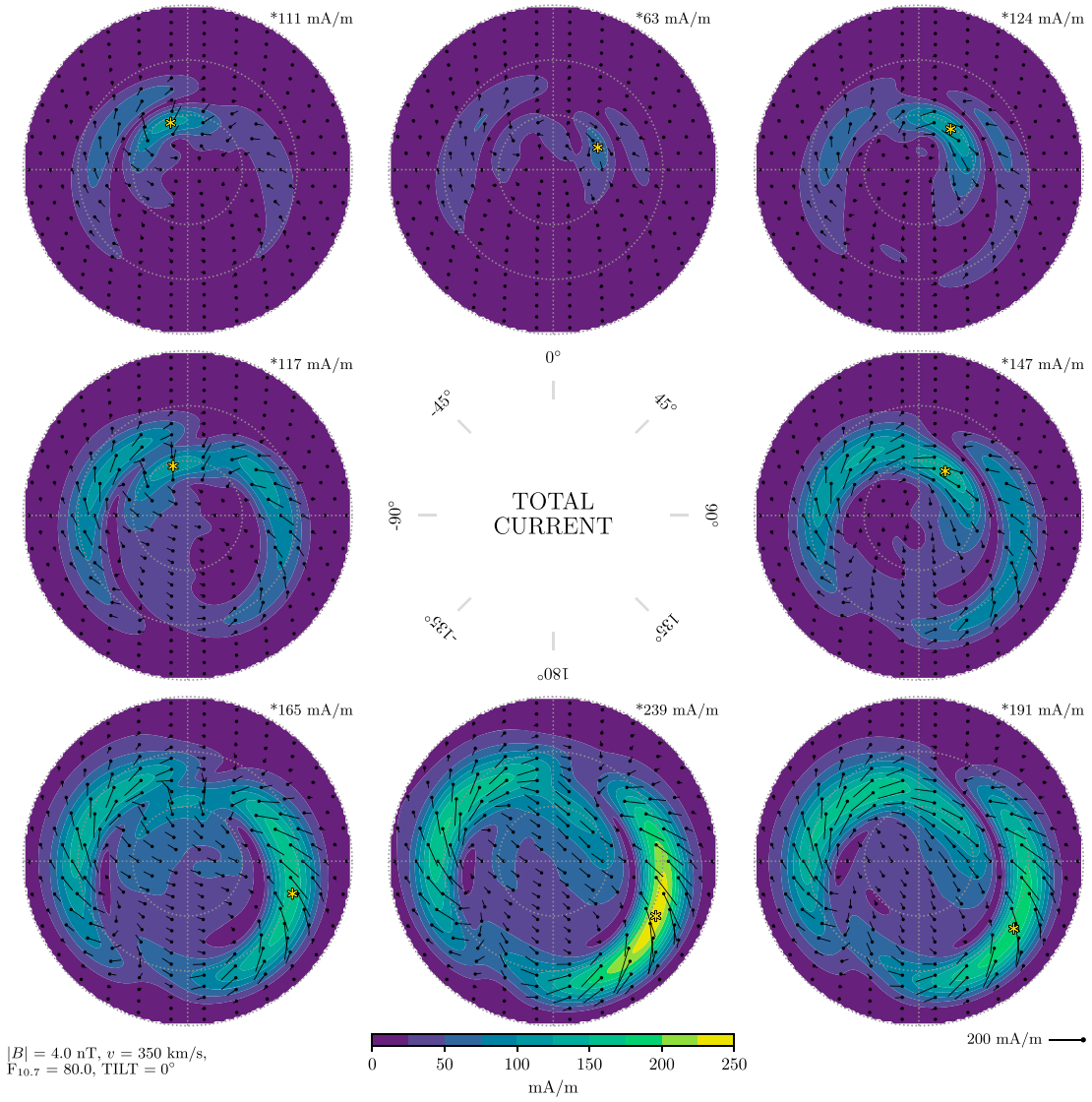

Figure 10. Same as Figure 9, only with tilt angle 0° (*equinox*).

The true current is of great importance in ionospheric electrodynamics. For example, knowledge about the current is necessary to estimate the energy dissipation, **E**·**J**, where **E** is the electric field in the frame of reference of the neutrals.

Figures 9–11 show maps of the total horizontal sheet current density in a similar format to the current densities shown in Figures 5–7. The colors denote the current magnitude, on a color scale which is common for all figures, and the pins show direction and magnitude relative to a reference in the lower right corners. The peak current in each plot is shown in the top right corner, and its location is indicated by a yellow star.

In winter, Figure 9, the polar cap is nearly void of current for all orientations of the IMF. For purely northward IMF, the model shows essentially no current at all. The current increases as the IMF rotates southward, but only in the auroral oval, and most strongly in the postmidnight region. The current in the Northern Hemisphere is significantly stronger for B_y positive conditions than for B_y negative. The direction of the current is primarily along the auroral oval, and it converges in the premidnight region, where the upward R1 current peaks in winter (Figure 5). In the postmidnight (premidnight) region, the current also has an equatorward (poleward) component, consistent with a current that links adjacent R1 and R2 Birkeland currents.

For equinox conditions (Figure 10), the currents during northward IMF are significantly stronger on the dayside compared to winter. This is very likely an effect of increased conductivity by ionization from sunlight.

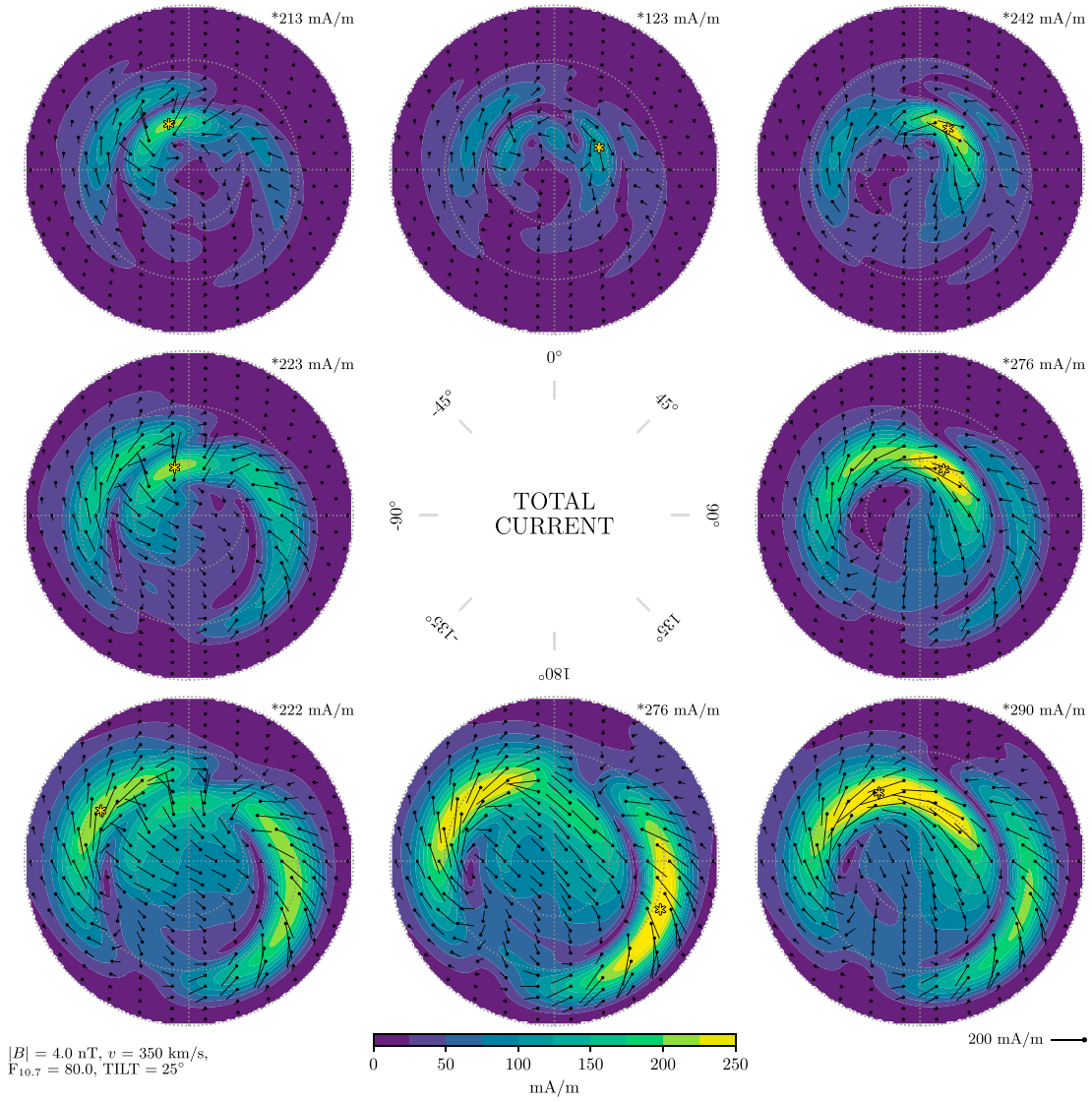

Figure 11. Same as Figure 9, only with tilt angle 25° (*summer*).

The location of the peak dayside current is strongly dependent on B_y and is located on the sunward portion of what looks like signatures of lobe convection cells (Förster et al., 2008) in the divergence-free current plots of Figure 6. This region is also sandwiched between upward and downward Birkeland currents, which connect horizontally by a current that is roughly perpendicular to the convection-aligned Hall currents.

The nightside currents are weak when the IMF is northward. When it rotates southward, the current magnitude increases at dawn and dusk. This is somewhat different from the winter patterns, where the dawn currents increase much more than the currents at dusk, indicating that the currents at dusk are more dependent on sunlight-produced conductivity than currents at dawn. When IMF B_z is negative, the dominating region is again postmidnight, where the peak westward electrojet is. The peak current is consistently stronger for B_y positive conditions. For southward IMF ($B_z < 0$), the currents in the polar cap are nonnegligible, and they point toward postnoon. This is consistent with a combination of sunward Hall currents and Pedersen currents that link the dawn and dusk R1 Birkeland currents. We return to this in section 4.3.

In summer (Figure 11), the currents on the dayside, at the dusk flank, and in the polar cap become much stronger, while the changes in the dawn currents are modest. The strongest currents appear near noon for all IMF orientations except strictly southward. The strongest peak current, across all plots in Figures 9–11, appear on the dayside when B_y is positive and B_z negative.

The only study that we know which presents similar maps of the total currents as those shown here, is by Friis-Christensen et al. (1984). Their maps were produced by combining Greenland ground magnetometer measurements, from the summer, with assumptions about ionospheric conductivity, using the technique by Kamide et al. (1981). Comparing their Figure 6 with our Figure 11, we see that they mostly agree. The main differences are that our polar cap currents rotate toward dusk as B_y goes from positive to negative, while the currents presented by Friis-Christensen et al. (1984) stay sunward. Also, for B_y positive and B_z zero, we find that the polar cap currents are confined mainly to the dawnside of the noon-midnight meridian, while Friis-Christensen et al. (1984) suggest significant sunward currents at dusk. The discrepancies are probably due to the conductivity models that they used, and differences between our divergence-free currents and their equivalent currents, derived from ground-based measurements. Their equivalent current (Figure 3 in their paper) deviate from our divergence-free currents (Figure 7) most notably by a clockwise rotation of the dusk current cell.

4. Discussion

In the previous section we established that the currents of Figures 5–7 largely reproduce previous results based on satellite measurements (Birkeland currents) and ground-based measurements (divergence-free horizontal currents). We also presented corresponding plots of the total horizontal sheet current density, calculated by combining the divergence-free sheet current and a curl-free sheet current derived from the Birkeland current density pattern.

We found that the horizontal current magnitudes are typically stronger when B_y is positive than when it is negative. On the dayside, the direction of the current is consistent with the so-called Svalgaard-Mansurov effect: eastward when B_y is positive, and westward when it is negative, opposite to the prevailing convection (Jørgensen et al., 1972). The asymmetries in magnitude may be an effect of a larger relative difference between the electron and neutral particle velocities when B_y is positive: The neutrals, to a first approximation, follow the Earth's eastward rotation, opposing the plasma flow imposed by solar wind interaction when B_y is positive, but not when it is negative (e.g., Haaland et al., 2007). Since the ions are more strongly coupled to the neutrals through collisions than the electrons, the larger velocity difference between the neutral and electron fluids means larger relative differences in ion and electron velocities, and hence currents.

We also found that in some regions, the dayside and dusk auroral oval and in the polar cap the currents are very sensitive to changes in solar irradiation. The current in the postmidnight auroral oval is much less sensitive to seasonal variations. The lack of seasonal variation suggests that this current is relatively unaffected by variations in sunlight-induced conductivity, and instead depends on conductivity caused by particle precipitation. Newell et al. (2010) showed that the postmidnight region and the dawn flank is where most diffuse electron precipitation takes place and that this precipitation is fairly independent of seasons. That is also consistent with the empirical model of ionospheric conductivity by Hardy et al. (1987).

The horizontal current peak in the postmidnight region coincides with what is often called the westward electrojet, most often in the context of equivalent currents measured from ground. In the following we discuss how the westward electrojet relates to true currents, and how its connection to Birkeland currents changes with seasons. We then give an interpretation of the winter current system, when the horizontal current is confined to the auroral oval. Finally, we compare the currents to a convection model (Weimer, 2005), to show how the roles of Hall and Pedersen currents change with seasons.

4.1. The Westward Electrojet

The westward electrojet is typically associated with southward ground magnetic field perturbations, corresponding to an equivalent westward overhead current. An increasing westward electrojet is a recurring signature of substorms (e.g., Akasofu, 1964), often used as their defining feature (e.g., Forsyth et al., 2015). It is monitored by the *AL* (Davis & Sugiura, 1966) and *SML* (Newell & Gjerloev, 2011) indices, and it can also be quantified on an orbit-by-orbit basis using low Earth orbiting spacecraft measurements of the absolute magnetic field disturbance (Aakjær et al., 2016; Olsen, 1996; Smith et al., 2017; Vennerstrom & Moretto, 2013). It is strongest in the postmidnight auroral zone (e.g., Laundal, Gjerloev, et al., 2016), and its average magnitude depends on the IMF B_y in opposite ways in summer and winter (Friis-Christensen et al., 2017). All these features are apparent also in the divergence-free currents of Figures 5–7, which we take to be approximately equal to the equivalent current observed from ground.

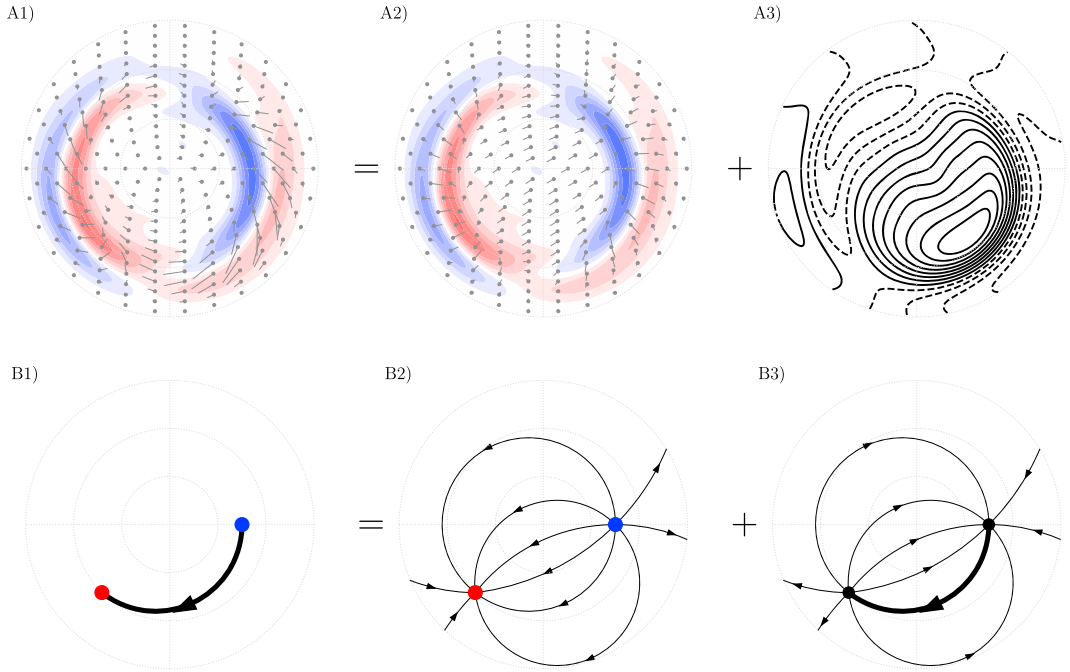

Figure 12. (A1) AMPS model Birkeland currents and horizontal currents for winter conditions, with southward IMF (4 nT). The horizontal current is a sum of a curl-free part (A2), and a divergence-free part (A3). Lower row: The same quantities as above, only in a simplified schematic representation, with Birkeland currents confined to two points, connected by a line current. The Helmholtz decomposition of this current system is shown in (B2) and (B3).

The interpretation of the westward electrojet can be ambiguous. It is often considered to be a Hall current associated with the sunward flow on the dawn flank, while its increase during substorms is a signature of a westward current connecting a pair of Birkeland currents that form the boundaries of a so-called substorm current wedge (McPherron et al., 1973). These two parts have been termed DP2 (convection-driven) and DP1 (substorm current wedge), respectively (see, e.g., review by Ganushkina et al., 2015). These interpretations are problematic when no other information than ground magnetic perturbations are available, because there is no way of distinguishing between them. With the present model, on the other hand, we can investigate directly how the westward electrojet relates to the true horizontal current, and how it connects to the Birkeland currents.

Figures 9–11 show that the postmidnight region is dominated by a strong horizontal current. Like the westward electrojet it has a modest variation with seasons, compared to currents elsewhere, and a strong dependence on B_y in the winter. It peaks at the latitude that separates R1 and R2 currents, which is also where the westward electrojet is strongest. The direction of the true current has a consistent southward rotation compared to the westward electrojet. This southward rotation is clearly due to a local closure current, connecting neighboring R1 and R2 currents, that is not part of the divergence-free current.

The westward electrojet extends farther across the midnight meridian in winter (Figure 5) than in summer (Figure 7). In winter, it extends far into the dusk R1 current, and turns northward near 21 MLT where the R1 current reaches a maximum. In summer, the electrojet aligns with the dawn R1 current, and turns northward near the boundary between the dawn and dusk R1 as expected. This is consistent with a Hall current in the expanding-contracting polar cap paradigm (Milan, 2013; Milan et al., 2017), and we show this more directly in section 4.3. Thus, while the magnitude of the westward electrojet is fairly constant, its location relative to the Birkeland current changes. We present an interpretation of the winter current pattern in the next section.

4.2. Understanding the Winter Current System

Figure 12 (A1) shows the Birkeland current pattern from Figure 5 (winter) for a purely southward directed IMF of 4 nT, with corresponding total horizontal current vectors (from Figure 9). This is the full current system. As explained earlier, the horizontal part can be decomposed in terms of a curl-free sheet current, shown in Figure 12 (A2), derived from the Birkeland currents, and a divergence-free part, displayed as contours

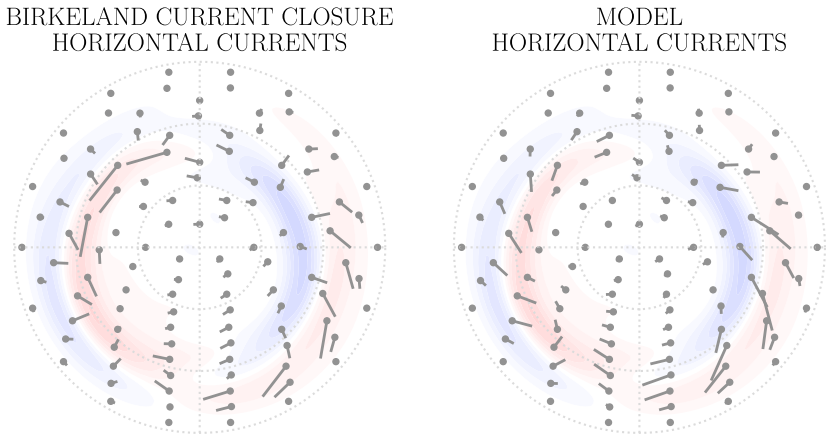

Figure 13. Birkeland current maps in northern winter with 180° clock angle (corresponding to the bottom center map of Figure 5), with horizontal currents estimated in two different ways. (left) Horizontal currents estimated purely by closing Birkeland currents through a spherical shell whose conductivity varies in proportional to upward Birkeland current magnitudes. (right) Horizontal currents from the model.

in Figure 12 (A3). Notice that neither the curl-free nor the divergence-free currents are zero in the polar cap but that their sum is. That means, as shown by Laundal et al. (2015), that ground magnetic field perturbations in the winter polar cap are nonzero but are caused by currents in the auroral oval instead of overhead currents.

In the lower row of Figure 12, we show a conceptual current system that captures some of the main features of the above maps, despite severe simplifications. Figure 12 (B1) shows a pair of Birkeland currents, leaving and entering the ionosphere in single points (red and blue dots). They have been placed near the peak Birkeland currents from the AMPS model, and they are connected by a horizontal line current that is mainly westward, located between the latitudes of the Birkeland currents.

The Helmholtz decomposition of this simple current system is not so simple, as shown to the right. The curl-free currents are here displayed as streamlines, which are analogous to electric field lines in a plane between two point charges. The divergence-free currents are closed loops that coincide at the Birkeland current points and along the true current path (thick streamline). Everywhere else the paths of the loops are opposite to the curl-free current streamlines. If the current of Figure 12 (B1) was the true current, the equivalent current derived from ground magnetometers would be as shown in Figure 12 (B3) (assuming radial field lines). The opposite is not true, however: the equivalent current in Figure 12 (B3) could correspond to the three-dimensional current of Figure 12 (B1), or an actual two-dimensional horizontal current that is equal to the equivalent current in Figure 12 (B3). Additional information is needed to separate between the two current geometries.

Even though the currents in the bottom row are extremely simplified, there are significant similarities with the model currents of the top row. Our interpretation is that the dominant winter current system is a pair of R1 currents and a horizontal closure along the auroral oval and that there is little or no contribution from an independently circulating current.

In Figure 13 we test this idea in a more realistic setup. The right part of the figure shows the same current system as in Figure 12 (A1) (winter, southward IMF). The horizontal currents to the left are calculated from the Birkeland current system, with the assumption that there is no additional current flow in the ionosphere. This is done by solving a set of equations based on Kirschoff's circuit laws: Birkeland currents from the model (shown in the background) leave or enter a set of nodes, evenly spaced in latitude and longitude, connected horizontally by wires. The conductivity of these wires is low and uniform, except where Birkeland currents flow upward, where the conductivity varies in proportion to the current. The wires connecting the nodes are both zonal and meridional, but the most poleward nodes are not connected across the pole. In the calculations, current densities are integrated over space, and then converted back to densities for presentation in Figure 13. While this setup is not meant to be a realistic representation of the ionosphere, the implied horizontal currents

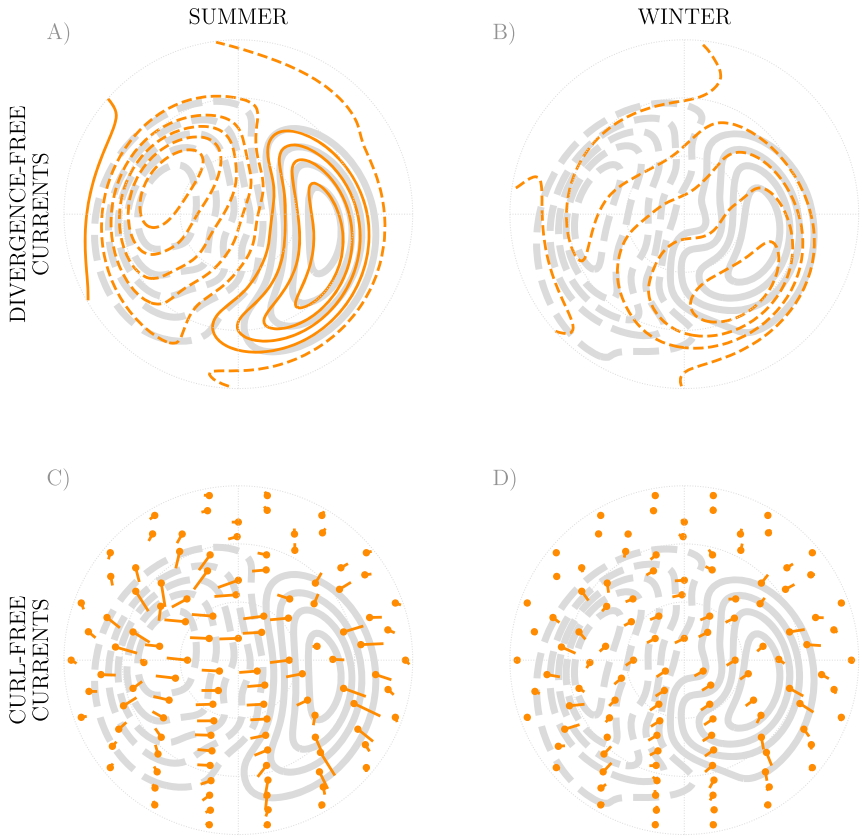

Figure 14. Weimer (2005) electric equipotential contours, in gray, from summer (left) and winter (right), and $B_z = -4$ nT, $B_y = 0$ nT. Equivalent current functions from the AMPS model (top) and curl-free currents (bottom) are shown for corresponding conditions. Both divergence-free current functions are normalized so that the summer current function has the same range as the summer electric potential. The potential contours are separated by 7 kV. All plots are in magnetic coordinates, with 12 MLT on top, looking down at the Northern Hemisphere, and circles of latitude shown every 10°. AMPS = Average Magnetic field and Polar current System; MLT = magnetic local time.

are guaranteed to be purely closure currents. The fact that the currents to the left and right in Figure 13 are so similar is evidence that the winter horizontal currents are predominantly part of the Birkeland current system, and that there is little contribution from an independent horizontal circulation. Our analyses show that this conclusion is independent of IMF orientation, except possibly during northward IMF when the winter currents are extremely weak.

4.3. Relation to Hall and Pedersen Currents

So far we have mostly avoided discussion of the Hall and Pedersen current components. The reason for this is that our model provides only the sum of these components; the decomposition into Pedersen and Hall components requires knowledge about the convection electric field. In this section, we compare the current patterns to an empirical model of the electric field, by Weimer (2005), in order to analyze seasonal variations in terms of Hall and Pedersen components.

In Figure 14 we compare model currents with Weimer (2005) convection patterns for southward IMF. In the top row, we show the divergence-free current function, and in the bottom row the curl-free currents. The left plots correspond to summer conditions in the north (tilt = 25°) and the right plots to winter (tilt = −25°). In all cases, and for both models, $B_y = 0$ nT, and $B_z = -4$ nT. The convection model values were calculated using the online tool by the Community Coordinated Modeling Center (ccmc.gsfc.nasa.gov) at Goddard Space Flight Center, and is displayed as gray contours.

The first thing that we notice is that in summer, the convection contours and the divergence-free current function contours are very well aligned. The curl-free currents are largely perpendicular to the convection contours. This means that the divergence-free current represents Hall currents, and the curl-free currents

are Pedersen currents. In this case, Hall currents circulate without connecting to Birkeland currents, and the Pedersen currents can be interpreted as the Birkeland closure current. This closure current connects the R1 currents to each other, across the polar cap, and to their neighboring R2 currents.

In winter, the situation changes dramatically. The differences in the convection are relatively modest, but the currents are significantly different. The dominating dawn cell aligns with convection only in the region of return flow at dawn, where the westward electrojet is. Thus, we conclude that this portion of the westward electrojet is a Hall current, just like in summer. The difference between winter and summer, as shown in section 4.2, is that in winter this Hall current connects to Birkeland currents. The curl-free current in this region is perpendicular to the divergence-free current, and to the equipotential contours, which means that it is a Pedersen current. Closer to midnight, however, the electrojet crosses equipotential contours, and the curl-free current is close to zero. That means that the electrojet represents mainly a Pedersen current in this region.

Away from the westward electrojet, the curl-free and divergence-free parts are not perpendicular, and interpretation in terms of Hall/Pedersen current components becomes complicated or meaningless.

5. Conclusions and Future Outlook

We have presented a new global model of the full ionospheric disturbance magnetic field and related ionospheric electric currents, based on magnetic field measurements from the Swarm and CHAMP satellites, in low Earth orbit. The model is parameterized by the following: dipole tilt angle, solar wind speed, IMF B_y and B_z, and the $F_{10.7}$ solar flux index. An important unique feature of this model is the consistent consideration of the magnetic fields associated with both the field-aligned and the divergence-free part of the horizontal current. This enables us to calculate the full horizontal current sheet density (which is not necessarily divergence-free since it is in part fed by the field-aligned currents), without additional assumptions about ionospheric electric conductivity or electric fields.

We have used this capability to investigate the full 3-D current system in the northern polar region, for different seasons and orientations of the IMF. We found that the horizontal current is generally stronger when B_y is positive than when it is negative. On the dayside, at high latitudes, where the currents become particularly strong; this may be an effect of a larger relative difference in plasma and neutral flows when B_y is positive than when it is negative. According to several statistical studies (e.g., Förster et al., 2008), the solar wind-driven plasma convection in this region is mostly westward when B_y is positive and eastward when it is negative. The westward convection is opposite to Earth's rotation, which presumably leads to larger differences between neutral and plasma velocities, and thus stronger currents, than eastward convection.

We also find that the horizontal currents in winter serve to close Birkeland currents, while in summer they have an additional part: Hall current vortices. The westward electrojet is mainly a Hall current in both seasons, according to a comparison with the Weimer (2005) electric field model, but its connection to other current systems changes: In winter it is part of a horizontal connection, along the auroral oval, between the R1 currents at dawn and dusk. In summer it is part of a horizontal circulation, without any significant vertical coupling.

All the results shown above were derived based on maps from the Northern Hemisphere. In the Southern Hemisphere, the maps would be largely the same if the signs of B_y and the dipole tilt angle were reversed. However, this symmetry is not exact. Since we do not impose any assumptions on the model symmetry, and since we take north-south differences in the Earth's main field into account, our model can be used to precisely compare hemispheres, and to test our understanding about hemispheric asymmetries. This will be the topic of a future publication.

The model can also be used to estimate ground magnetic field perturbations, by making an assumption about the height of the ionospheric horizontal current sheet and about the effects of ground induction. This will again be explored in future publications.

We also invite the scientific community to make use of open-source Python code to calculate model currents and magnetic fields (Laundal & Toresen, 2018).

Appendix A: Model Derivation

In this appendix we present the technique that we use to relate the model coefficients to magnetic field disturbances at low Earth orbit. The relationship between the magnetic field and model coefficients can be formulated as a set of linear equations,

$$\mathbf{d} = \mathbf{G}\mathbf{m} \tag{A1}$$

where **d** is a vector of magnetic field components, **m** a vector of model coefficients, and **G** is a matrix relating **m** and **d**. In section A1 we present the equations used to construct **G**, and in section A2 we present the technique that we use for the inverse problem of estimating **m** from a set of measurements **d**. The equations are largely similar to what was presented by Laundal, Finlay, et al. (2016), and we refer to that paper, and references therein, for details and derivations.

A1. Mathematical Formulation

The magnetic perturbation field, $\Delta\mathbf{B}$, can be decomposed as a sum of poloidal and toroidal parts, which are represented by scalars that we call V and T, respectively (see equation (1)). We expand V and T in series of spherical harmonics:

$$V(\lambda_q, \phi_{\text{mlt}}, h) = R_E \sum_{n,m} \left(\frac{R_E}{R_E + h}\right)^{n+1} P_n^m(\sin\lambda_q)[g_n^m \cos(m\phi_{\text{mlt}}) + h_n^m \sin(m\phi_{\text{mlt}})], \tag{A2}$$

$$T(\lambda_m, \phi_{\text{mlt}}) = \sum_{n,m} P_n^m(\sin\lambda_m)[\psi_n^m \cos(m\phi_{\text{mlt}}) + \eta_n^m \sin(m\phi_{\text{mlt}})], \tag{A3}$$

where the spherical harmonic coefficients, g_n^m, h_n^m, ψ_n^m, and η_n^m are functions of specific external parameters, as described in section 2. R_E is the Earth's radius (6,371.2 km), and h is geodetic height. $P_n^m(\sin\lambda_q) = P_n^m(\cos\theta_q)$ are Schmidt seminormalized associated Legendre functions of degree n and order m. λ_q is QD latitude, with colatitude $\theta_q = 90 - \lambda_q$, and λ_m is MA latitude. QD and MA coordinates are variants of apex coordinate systems, defined by Richmond (1995). The longitudinal parameter, ϕ_{mlt}, is the magnetic local time as defined by Laundal and Richmond (2017, equation 93), using QD/MA longitudes (which are equal). QD and MA coordinates are nonorthogonal, and so differentiation of V and T involves base vectors which depend on the local structure of the Earth's main magnetic field. The relevant base vectors are called $\mathbf{f}_i$ and $\mathbf{d}_i$ below, and are calculated using a code published by Emmert et al. (2010), accessed through the Python wrapper available at https://github.com/cmeeren/apexpy. We use the following expressions (Laundal, Finlay, et al., 2016) for the geodetic eastward (subscript e), northward (n), and upward (u) components, respectively:

$$\begin{aligned}\Delta B_e = &\frac{-d_{1,n}}{\cos\lambda_m}\frac{\partial T}{\partial\phi_{\text{mlt}}} \\ &+ \frac{d_{2,n}}{\sin I_m}\frac{\partial T}{\partial\lambda_m} \\ &- \frac{f_{2,n}}{R_E + h}\frac{1}{\cos\lambda_q}\frac{\partial V}{\partial\phi_{\text{mlt}}} \\ &+ \frac{f_{1,n}}{R_E + h}\frac{\partial V}{\partial\lambda_q}\end{aligned} \tag{A4}$$

$$\begin{aligned}\Delta B_n = &\frac{d_{1,e}}{\cos\lambda_m}\frac{\partial T}{\partial\phi_{\text{mlt}}} \\ &- \frac{d_{2,e}}{\sin I_m}\frac{\partial T}{\partial\lambda_m} \\ &+ \frac{f_{2,e}}{R_E + h}\frac{1}{\cos\lambda_q}\frac{\partial V}{\partial\phi_{\text{mlt}}} \\ &- \frac{f_{1,e}}{R_E + h}\frac{\partial V}{\partial\lambda_q}\end{aligned} \tag{A5}$$

$$\Delta B_u = -\sqrt{F}\frac{\partial V}{\partial h} \tag{A6}$$

where $F = f_{1,e}f_{2,n} - f_{1,n}f_{2,e}$ (the upward component of $\mathbf{f}_1 \times \mathbf{f}_2$) and

$$\sin I_m = \frac{2\sin\lambda_m}{\sqrt{4 - 3\cos^2\lambda_m}}. \tag{A7}$$

Equations (1) and (A2)–(A7), together with equations (2)–(5), can be combined to relate the magnetic disturbance field, $\Delta\mathbf{B}$, to the coefficients $h^m_{n,i}$, $g^m_{n,i}$, $\eta^m_{n,i}$, and $\psi^m_{n,i}$, $i = 1, 2, \ldots, 19$. The total number of coefficients depends on the truncation levels for spherical harmonic degree and order, chosen in equations (A2) and A3. We choose $N_V, M_V = 45, 3$, and $N_T, M_T = 65, 3$, which leads to a total of 758 terms in the spherical harmonic representations, each of which depends on 19 parameters [equation (2)]. In total, the model thus has 14,402 parameters.

A2. Derivation of Model Coefficients

The equations in the previous section, and in section 2, can be used to construct the matrix $\mathbf{G}$ of equation (A1). With the chosen expansion and truncation levels, $\mathbf{m}$ has 14,402 elements, which we estimate from 50,518,182 measured disturbance magnetic field vector components, measured by the CHAMP and Swarm satellites, using least squares. See section 2 for details about data selection and preprocessing.

The overdetermined set of equations in (A1) is solved by iteratively reweighted least squares, explained here in detail. First, we multiply equation (A1) by a diagonal weight matrix $\mathbf{W}^s$, whose elements are 1 for the data corresponding to CHAMP and Swarm Bravo measurements, and 0.5 for those corresponding to Swarm Alpha and Charlie measurements. This weighting is introduced because Alpha and Charlie fly side by side and therefore do not provide independent measurements at the scales resolved by the model. Then we multiply the equation by $\mathbf{G}^\top$ in order to obtain the normal equations of the least squares problem. An initial solution can be written as

$$\mathbf{m}_0 = (\mathbf{G}^\top\mathbf{W}^s\mathbf{G} + \mathbf{R})^{-1}\mathbf{G}^\top\mathbf{W}^s\mathbf{d}. \tag{A8}$$

Here we have also introduced an $U \times U$ diagonal model regularization matrix $\mathbf{R}$, where $U = 14,402$ is the number of unknowns. The regularization matrix is zero everywhere except at the diagonal elements corresponding to $\psi^m_{n,i}$ and $\eta^m_{n,i}$. These elements are $\kappa^2 n(n+1)/(2n+1)$, where κ^2 is a small regularization parameter. Equation (A8) is solved using Cholesky decomposition, using the Python Scipy library, which calls the LAPACK library (E. Anderson et al., 1999). This is only possible if $\mathbf{G}^\top\mathbf{W}^s\mathbf{G} + \mathbf{R}$ is not singular. We choose the smallest value for the regularization parameter κ^2, in powers of 10, for which $\mathbf{G}^\top\mathbf{W}^s\mathbf{G}+\mathbf{R}$ is invertible. No regularization is needed for the poloidal field parameters. The need for regularization in the toroidal parameters probably has to do with the facts that (1) modified apex coordinates do not cover the whole globe at satellite height (equatorial latitudes are missing, as seen in Figure 1), and (2) near the equator the latitudinal variation of T is not well constrained [see equations (A4) and (A5)], since $d_{2,e}$ and $d_{2,n}$ are very small there. While T will be defined at low latitudes, we do not expect it to be physically meaningful there (meaning that vertical currents at low latitudes are not resolved). There is no exact boundary where T becomes meaningful, but a reasonable cutoff is 45°.

In the next steps, we introduce an additional set of weights according to the data misfit in the previous iteration. With $\mathbf{m}_j$ as the solution of the jth iteration, we calculate residuals, $\mathbf{e}_j = \mathbf{d} - \mathbf{G}\mathbf{m}_j$. Based on these, a set of Huber weights (Huber, 1964) is calculated,

$$w^i_j = \min(1, 1.5\sigma_j/|e^i_j|) \tag{A9}$$

where e^i_j is the ith elements in $\mathbf{e}_j$. σ_j is the root-mean-square of the elements in $\mathbf{e}_j$, where the mean is also calculated robustly, using iterative reweighting by Huber weights. The $(j+1)$th iteration for the model parameter vector can be written as

$$\mathbf{m}_{j+1} = (\mathbf{G}^\top\mathbf{W}^h_j\mathbf{W}^s\mathbf{G} + \mathbf{R})^{-1}\mathbf{G}^\top\mathbf{W}^h_j\mathbf{W}^s\mathbf{d}. \tag{A10}$$

where $\mathbf{W}_j^h$ is a diagonal weight matrix of Huber weights, calculated by (A9) using the residuals from the jth iteration. The final solution was achieved when $\|\mathbf{m}_{j-1} - \mathbf{m}_j\| < 10^{-2}\|\mathbf{m_0}\|$, after 12 iterations.

This iterative technique reduces the effect of outliers, so that the final solution better represents typical values, which may be different from the arithmetic mean. The currents will typically be weaker and smoother in later iteration steps than they are in the first step.

Appendix B: Relation to Ionospheric Currents

In section 2 and in Appendix A, we explain how the model coefficients are related to the magnetic field in near-Earth space, and how we use measurements of the magnetic field from low Earth orbit to estimate the model coefficients. Yet when we present model results in section 3, we present them in terms of ionospheric currents. In this appendix we explain how the currents are derived from the model coefficients. The currents are essentially calculated from $\nabla \times \Delta\mathbf{B}/\mu_0$, treating the apex coordinates as orthogonal spherical coordinates, and $h + R_E$ as the geocentric radius. Again, we refer to Laundal, Finlay, et al. (2016), and references therein, for details and derivations.

The currents are calculated at the height h_R, which is also the reference height in the modified apex coordinate system. This height is a matter of choice/assumption, and changing it changes the currents. This ambiguity/freedom is not present in the magnetic field description of Appendix A. For all currents in this paper, we have chosen $h_R = 110$ km.

At $h = h_R$, $\lambda_q = \lambda_m$, so we skip the subscripts. We give the units for each quantity, assuming that μ_0 is provided in units of Tm/A, and R_E, h_R in units of kilometer. The spherical harmonic coefficients have units nanotesla.

The vertical current density (unit μA/m^2) is

$$J_u(\lambda, \phi_{\text{mlt}}) = -\frac{10^{-6}}{\mu_0(R_E + h_R)} \sum_{n,m} n(n+1) P_n^m(\sin\lambda) \left[\psi_n^m \cos m\phi_{\text{mlt}} + \eta_n^m \sin m\phi_{\text{mlt}}\right] \tag{B1}$$

The horizontal sheet current density is

$$\mathbf{J} = \mathbf{J}_{\text{df}} + \mathbf{J}_{\text{cf}} = \mathbf{k} \times \nabla\Psi + \nabla\alpha, \tag{B2}$$

where we have written $\mathbf{J}_{\text{df}}$ in terms of a scalar field Ψ, and $\mathbf{J}_{\text{cf}}$ in terms of a scalar field α. $\mathbf{k}$ is an upward unit vector.

The scalar for the divergence-free part, the current function Ψ (unit μA) is

$$\Psi(\lambda, \phi_{\text{mlt}}) = -\frac{R_E}{\mu_0} \sum_{n,m} \frac{2n+1}{n} \left(\frac{R_E}{R_E + h_R}\right)^{n+1} P_n^m(\sin\lambda) \left[g_n^m \cos m\phi_{\text{mlt}} + h_n^m \sin m\phi_{\text{mlt}}\right] \tag{B3}$$

This equation for Ψ corresponds to an equivalent current function of internal origin, as described in Chapman and Bartels (1940).

The scalar for the curl-free part α (unit μA) is

$$\alpha(\lambda, \phi_{\text{mlt}}) = -\frac{R_E + h_R}{\mu_0} \sum_{n,m} P_n^m(\sin\lambda) \left[\psi_n^m \cos m\phi_{\text{mlt}} + \eta_n^m \sin m\phi_{\text{mlt}}\right] \tag{B4}$$

Note that there is a sign error in the corresponding equation (22) in Laundal, Finlay, et al. (2016), which has been corrected here.

From the preceding equations, we get the following expressions for the magnetic eastward and northward components of the ionospheric sheet current densities $\mathbf{J}_{\text{df}}$ and $\mathbf{J}_{\text{cf}}$ (unit mA/m):

$$J_{\text{df},e} = \frac{10^{-6}}{\mu_0} \sum_{n,m} \left(\frac{R_E}{R_E + h_R}\right)^{n+2} \frac{2n+1}{n} \frac{dP_n^m(\sin\lambda)}{d\lambda} [g_n^m \cos(m\phi_{\text{mlt}}) + h_n^m \sin(m\phi_{\text{mlt}})] \tag{B5}$$

$$J_{\mathrm{df},n} = \frac{10^{-6}}{\mu_0 \cos\lambda} \sum_{n,m} \left(\frac{R_E}{R_E + h_R} \right)^{n+2} \frac{2n+1}{n} P_n^m(\sin\lambda) m [g_n^m \sin(m\phi_{\mathrm{mlt}}) - h_n^m \cos(m\phi_{\mathrm{mlt}})] \quad \text{(B6)}$$

$$J_{\mathrm{cf},e} = \frac{10^{-6}}{\mu_0 \cos\lambda} \sum_{n,m} P_n^m(\sin\lambda) m [\psi_n^m \sin(m\phi_{\mathrm{mlt}}) - \eta_n^m \cos(m\phi_{\mathrm{mlt}})] \quad \text{(B7)}$$

$$J_{\mathrm{cf},n} = -\frac{10^{-6}}{\mu_0} \sum_{n,m} \frac{dP_n^m(\sin\lambda)}{d\lambda} [\psi_n^m \cos(m\phi_{\mathrm{mlt}}) + \eta_n^m \sin(m\phi_{\mathrm{mlt}})] \quad \text{(B8)}$$

The total horizontal eastward sheet current density is (B5) + (B7), and the northward is (B6) + (B8).

Acknowledgments
ESA is thanked for providing prompt access to the Swarm L1b data, accessible at http://earth.esa.int/swarm. The support of the CHAMP mission by the German Aerospace Center (DLR) and the Federal Ministry of Education and Research is gratefully acknowledged. CHAMP magnetic field measurements are available through the Information System and Data Center, ISDC, at http://isdc.gfz-potsdam.de. The IMF, solar wind, and magnetic index data were provided through OMNIWeb by the Space Physics Data Facility(SPDF), and downloaded from ftp://spdf.gsfc.nasa.gov/pub/data/omni/highresomni/. We thank the AMPERE team and the AMPERE Science Center for providing the Iridium derived data products (data available from http://ampere.jhuapl.edu/). K. M. L. and J. P. R. were funded by the Research Council of Norway/CoE under contract 223252/F50. The study is also funded by ESA through the Swarm Data Innovation and Science Cluster (Swarm DISC) within the reference frame of ESA contract 000109587/13/I-NB. For more information on Swarm DISC, please visit https://earth.esa.int/web/guest/missions/esa-eo-missions/swarm/disc.

References

Aakjær, C. D., Olsen, N., & Finlay, C. C. (2016). Determining polar ionospheric electrojet currents from Swarm satellite constellation magnetic data. *Earth Planets Space*, *68*, 140. https://doi.org/10.1186/s40623-016-0509-y

Akasofu, S.-I. (1964). The development of the auroral substorm. *Planetary and Space Science*, *12*, 273–282.

Amm, O. (1997). Ionospheric elementary current systems in spherical coordinates and their application. *Journal of Geomagnetism and Geoelectricity*, *49*(7), 947–955.

Anderson, B. J., Korth, H., Waters, C. L., Green, D. L., & Stauning, P. (2008). Statistical Birkeland current distributions from magnetic field observations by the Iridium constellation. *Annales Geophysicae*, *26*, 671–687.

Anderson, B. J., Takahashi, K., & Toth, B. A. (2000). Sensing global Birkeland currents with iridium engineering magnetometer data. *Geophysical Research Letters*, *27*, 4045–4048.

Anderson, E., Bai, Z., Bischof, C., Blackford, S., Demmel, J., Dongarra, J., et al. (1999). *LAPACK users' guide* (3rd ed.). Philadelphia, PA: Society for Industrial and Applied Mathematics.

Backus, G. (1986). Poloidal and toroidal fields in geomagnetic field modeling. *Reviews of Geophysics*, *24*, 75–109.

Birkeland, K. (1901). Résultats des rescherches magnéthiques faites par l'expédition Norvégienne de 1899–1900. *Archives des Sciences Physiques et Naturelles*, 565–586.

Chapman, S., & Bartels, J. (1940). *Geomagnetism* (Vol. 2). London, UK: Oxford University Press.

Coxon, J. C., Milan, S. E., Carter, J. A., Clausen, L. B. N., Anderson, B. J., & Korth, H. (2016). Seasonal and diurnal variations in AMPERE observations of the Birkeland currents compared to modelled results. *Journal of Geophysical Research*, *121*, 4027–4040. https://doi.org/10.1002/2015JA022050

Crooker, N. U., & Rich, F. J. (1993). Lobe cell convection as a summer phenomenon. *Journal of Geophysical Research*, *98*(A8), 13,403–13,407. https://doi.org/10.1029/93JA01037

Davis, T. N., & Sugiura, M. (1966). Auroral electrojet activity index AE and its universal time variations. *Journal of Geophysical Research*, *71*, 785–801.

Detman, T. R., & Vassiliadis, D. (1997). *Review of techniques for magnetic storm forecasting* (pp. 253–266). Washington, DC: American Geophysical Union. https://doi.org/10.1029/GM098p0253

Egeland, A., & Burke, W. J. (2010). Kristian Birkeland's pioneering investigations of geomagnetic disturbances. *History of Geo- and Space Sciences*, *1*, 13–24. https://doi.org/10.5194/hgss-1-13-2010

Emmert, J. T., Richmond, A. D., & Drob, D. P. (2010). A computationally compact representation of magnetic apex and quasi dipole coordinates with smooth base vectors. *Journal of Geophysical Research*, *115*, A08322. https://doi.org/10.1029/2010JA015326

Finlay, C. C., Olsen, N., Kotsiaros, S., Gillet, N., & Tøffner-Clausen, L. (2016). Recent geomagnetic secular variation from Swarm and ground observatories as estimated in the CHAOS-6 geomagnetic field model. *Earth, Planets and Space*, *68*, 112. https://doi.org/10.1186/s40623-016-0486-1

Förster, M., Haaland, S. E., Paschmann, G., Quinn, J. M., Torbert, R. B., Vaith, H., & Kletzing, C. A. (2008). High-latitude plasma convection during northward IMF as derived from in-situ magnetospheric Cluster EDI measurements. *Annales Geophysicae*, *26*, 2685–2700.

Forsyth, C., Rae, I. J., Coxon, J. C., Freeman, M. P., Jackman, C. M., Gjerloev, J., & Fazakerley, A. N. (2015). A new technique for determining substorm onsets and phases from indices of the electrojet (SOPHIE). *Journal of Geophysical Research: Space Physics*, *120*, 10,592–10,606. https://doi.org/10.1002/2015JA021343

Friis-Christensen, E., Finlay, C. C., Hesse, M., & Laundal, K. M. (2017). Magnetic field perturbations from currents in the dark polar regions during quiet geomagnetic conditions. *Space Science Reviews*, *206*, 281–297. https://doi.org/10.1007/s11214-017-0332-1

Friis-Christensen, E., Kamide, Y., Richmond, A. D., & Matsushita, S. (1984). Interplanetary magnetic field control of high-latitude electric fields and currents determined from greenland magnetometer data. *Journal of Geophysical Research*, *90*, 1325–1338.

Friis-Christensen, E., Lühr, H., & Hulot, G. (2006). Swarm: A constellation to study the Earth's magnetic field. *Earth Planets Space*, *58*(4), 351–358. https://doi.org/10.1186/BF03351933

Friis-Christensen, E., & Wilhjelm, J. (1975). Polar cap currents for different directions of the interplanetary magnetic field in the y-z plane. *Journal of Geophysical Research*, *80*, 1248–1260. https://doi.org/10.1029/JA080i010p01248

Fukushima, N. (1976). Generalized theorem for no ground magnetic effect of vertical currents connected with Pedersen currents in the uniform-conductivity ionosphere. *The Rise of Space Weather Research in Japan*, *30*, 35–50.

Ganushkina, N. Y., Liemohn, M. W., Dubyagin, S., Daglis, I. A., Dandouras, I., Zeeuw, D. L. D., et al. (2015). Defining and resolving current systems in geospace. *Annales Geophysicae*, *33*(11), 1369–1402. https://doi.org/10.5194/angeo-33-1369-2015

Green, D. L., Waters, C. L., Anderson, B. J., & Korth, H. (2009). Seasonal and interplanetary magnetic field dependence of the field-aligned currents for both Northern and Southern Hemispheres. *Annales Geophysicae*, *27*, 1701–1715. https://doi.org/10.5194/angeo-27-1701-2009

Green, D. L., Waters, C. L., Korth, H., Anderson, B. J., Ridley, A. J., & Barnes, R. J. (2007). Technique: Large-scale ionospheric conductance estimated from combined satellite and ground-based electromagnetic data. *Journal of Geophysical Research*, *112*, A05303. https://doi.org/10.1029/2006JA012069

Haaland, S. E., Paschmann, G., Förster, M., Quinn, J. M., Torbert, R. B., McIlwain, C. E., et al. (2007). High-latitude plasma convection from Cluster EDI measurements: Method and IMF-dependence. *Annales Geophysicae*, *25*, 239–253. https://doi.org/10.5194/angeo-25-239-2007

Hardy, D. A., Gussenhoven, M. S., Raistrick, R., & McNeil, W. J. (1987). Statistical and functional representation of the pattern of auroral energy flux, number flux, and conductivity. *Journal of Geophysical Research*, *92*, 12,275–12,294.

He, M., Vogt, J., Lühr, H., Sorbalo, E., Blagau, A., Le, G., & Lu, G. (2012). A high-resolution model of field-aligned currents through empirical orthogonal functions analysis (MFACE). *Geophysical Research Letters*, *39*, L18105. https://doi.org/10.1029/2012GL053168

Huber, P. J. (1964). Robust estimation of location parameter. *Annals of Mathematical Statistics*, *35*, 73–101.

Hubert, B., Milan, S. E., Grocott, A., Cowley, S. W. H., & Gérard, J. C. (2006). Dayside and nightside reconnection rates inferred from IMAGE-FUV and Super Dual Auroral Radar Network data. *Journal of Geophysical Research*, *111*, A03217. https://doi.org/10.1029/2005JA011140

Iijima, T., & Potemra, T. A. (1976). The amplitude distribution of field-aligned currents at northern high latitudes observed by triad. *Journal of Geophysical Research*, *81*, 2165–2174.

Iijima, T., & Potemra, T. A. (1978). Large-scale characteristics of field-aligned currents associated with substorms. *Journal of Geophysical Research*, *83*, 599–615.

Jørgensen, T. S., Friis-Christensen, E., & Wilhjelm, J. (1972). Interplanetary magnetic-field directions and high-latitude ionospheric currents. *Journal of Geophysical Research*, *77*, 1976–1977. https://doi.org/10.1029/JA077i010p01976

Juusola, L., Milan, S. E., Lester, M., Grocott, A., & Imber, S. M. (2014). Interplanetary magnetic field control of the ionospheric field-aligned current and convection distributions. *Journal of Geophysical Research*, *119*, 3130–3149. https://doi.org/10.1002/2013JA019455

Kamide, Y., Richmond, A. D., & Matsushita, S. (1981). Estimation of ionospheric electric fields, ionospheric currents, and field-aligned currents from ground magnetic records. *Journal of Geophysical Research*, *86*, 801–813. https://doi.org/10.1029/JA086iA02p00801

King, J., & Papitashvili, N. E. (2005). Solar wind spatial scales in and comparisons of hourly Wind and ACE plasma and magnetic field data. *Journal of Geophysical Research*, *110*, A02104. https://doi.org/10.1029/2004JA01064

Laundal, K. M., Finlay, C. C., & Olsen, N. (2016). Sunlight effects on the 3D polar current system determined from low Earth orbit measurements. *Earth Planets Space*, *68*(1), 142. https://doi.org/10.1186/s40623-016-0518-x

Laundal, K. M., Gjerloev, J. W., Ostgaard, N., Reistad, J. P., Haaland, S. E., Snekvik, K., et al. (2016). The impact of sunlight on high-latitude equivalent currents. *Journal of Geophysical Research: Space Physics*, *121*, 2715–2726. https://doi.org/10.1002/2015JA022236

Laundal, K. M., Haaland, S. E., Lehtinen, N., Gjerloev, J. W., Ostgaard, N., Tenfjord, P., et al. (2015). Birkeland current effects on high-latitude ground magnetic field perturbations. *Geophysical Research Letters*, *42*, 7248–7254. https://doi.org/10.1002/2015GL065776

Laundal, K. M., & Richmond, A. D. (2017). Magnetic coordinate systems. *Space Science Reviews*, *206*, 27–59. https://doi.org/10.1007/s11214-016-0275-y

Laundal, K. M., & Toresen, M. (2018). pyAMPS, https://github.com/klaundal/pyAMPS, https://doi.org/10.5281/zenodo.1182930

McPherron, R. L., Russell, C. T., & Aubry, M. P. (1973). Satellite studies of magnetospheric substorms on August 15, 1968: 9. Phenomenological Model for Substorms. *Journal of Geophysical Research*, *78*, 3131–3149. https://doi.org/10.1029/JA078i016p03131

Milan, S. E. (2013). Modeling Birkeland currents in the expanding/contracting polar cap paradigm. *Journal of Geophysical Research: Space Physics*, *118*, 5532–5542. https://doi.org/10.1002/jgra.50393

Milan, S. E., Clausen, L. B. N., Coxon, J. C., Carter, J. A., Walach, M.-T., Laundal, K., et al. (2017). Overview of solar wind–magnetosphere–ionosphere–atmosphere coupling and the generation of magnetospheric currents. *Space Science Reviews*, *206*, 547–573. https://doi.org/10.1007/s11214-017-0333-0

Newell, P. T., & Gjerloev, J. W. (2011). Evaluation of SuperMAG auroral electrojet indices as indicators of substorms and auroral power. *Journal of Geophysical Research*, *116*, A12211. https://doi.org/10.1029/2011JA016779

Newell, P. T., Sotirelis, T., Liou, K., Meng, C. I., & Rich, F. J. (2007). A nearly universal solar wind-magnetosphere coupling function inferred from 10 magnetospheric state variables. *Journal of Geophysical Research*, *112*, A01206. https://doi.org/10.1029/2006JA012015

Newell, P. T., Sotirelis, T., & Wing, S. (2010). Seasonal variations in diffuse, monoenergetic, and broadband aurora. *Journal of Geophysical Research*, *115*, A03216. https://doi.org/10.1029/2009JA014805

Ohtani, S., Ueno, G., & Higuchi, T. (2005). Comparison of large-scale field-aligned currents under sunlit and dark ionospheric conditions. *Journal of Geophysical Research*, *110*, A09230. https://doi.org/10.1029/2005JA011057

Olsen, N. (1996). A new tool for determining ionospheric currents from magnetic satellite data. *Geophysical Research Letters*, *23*(24), 3635–3638. https://doi.org/10.1029/96GL02896

Olsen, N. (1997). Ionospheric F region currents at middle and low latitudes estimated from Magsat data. *Journal of Geophysical Research*, *102*, 4563–4576.

Papitashvili, V. O., Christiansen, F., & Neubert, T. (2002). A new model of field-aligned currents derived from high-precision satellite magnetic field data. *Geophysical Research Letters*, *29*, 1683. https://doi.org/10.1029/2001GL014207

Pettigrew, E. D., Shepherd, S. G., & Ruohoniemi, J. M. (2010). Climatological patterns of high-latitude convection in the Northern and Southern Hemispheres: Dipole tilt dependencies and interhemispheric comparison. *Journal of Geophysical Research*, *115*, A07305. https://doi.org/10.1029/2009JA014956

Reigber, C., Lühr, H., & Schwintzer, P. (2002). CHAMP mission status. *Advances in Space Research*, *30*(2), 129–134. https://doi.org/10.1016/S0273-1177(02)00276-4

Richmond, A. D. (1995). Ionospheric electrodynamics. In H. Volland (Ed.), *Handbook of Atmospheric Electrodynamics* (Vol. 2, pp. 249–290). Boca Raton, FL: CRC Press.

Smith, A. R. A., Beggan, C. D., Macmillan, S., & Whaler, K. A. (2017). Climatology of the auroral electrojets derived from the along-track gradient of magnetic field intensity measured by POGO, Magsat, CHAMP, and Swarm. *Space Weather*, *15*, 1257–1269. https://doi.org/10.1002/2017SW001675

Snekvik, K., Østgaard, N., Tenfjord, P., Reistad, J. P., Laundal, K. M., Milan, S. E., & Haaland, S. E. (2017). Dayside and nightside magnetic field responses at 780 km altitude to dayside reconnection. *Journal of Geophysical Research: Space Physics*, *122*, 1670–1689. https://doi.org/10.1002/2016JA023177

Vanhamäki, H., & Amm, O. (2011). Analysis of ionospheric electrodynamic parameters on mesoscales—A review of selected techniques using data from ground-based observation networks and satellites. *Annales Geophysicae*, *29*, 467–491. https://doi.org/10.5194/angeo-29-467-2011

Vasyliunas, V. M. (1999). A note on current closure. *Journal of Geophysical Research*, *104*, 25,143–25,144.

Vasyliunas, V. M. (2007). The mechanical advantage of the magnetosphere: Solar-wind-related forces in the magnetosphere-ionosphere-Earth system. *Annales Geophysicae*, *25*, 255–269. https://doi.org/10.5194/angeo-25-255-2007

Vennerstrom, S., & Moretto, T. (2013). Monitoring auroral electrojets with satellite data. *Space Weather*, *11*, 509–519. https://doi.org/10.1002/swe.20090

Vestine, E. H., Laporte, L., Lange, I., & Scott, W. E. (1947). *The geomagnetic field, its description and analysis*. Washington, DC: Carnegie Institution of.

Waters, C. L., Anderson, B. J., & Liou, K. (2001). Estimation of global field aligned currents using the iridium system magnetometer data. *Geophysical Research Letters*, *28*, 2165–2168.

Waters, C. L., Gjerloev, J. W., Dupont, M., & Barnes, R. J. (2015). Global maps of ground magnetometer data. *Journal of Geophysical Research: Space Physics*, *120*, 9651–9660. https://doi.org/10.1002/2015JA021596

Weimer, D. (2001). Maps of ionospheric field-aligned currents as a function of the interplanetary magnetic field derived from Dynamics Explorer 2. *Journal of Geophysical Research*, *106*, 12,889–12,902.

Weimer, D. R. (2005). Improved ionospheric electrodynamic models and application to calculating joule heating rates. *Journal of Geophysical Research*, *110*, A05306. https://doi.org/10.1029/2004JA010884

Weimer, D. R. (2013). An empirical model of ground-level geomagnetic perturbations. *Space Weather*, *11*, 107–120. https://doi.org/10.1002/swe.20030

Weimer, D. R., Clauer, C. R., Engebretson, M. J., Hansen, T. L., Gleisner, H., Mann, I., & Yumoto, K. (2010). Statistical maps of geomagnetic perturbations as a function of the interplanetary magnetic field. *Journal of Geophysical Research*, *115*, A10320. https://doi.org/10.1029/2010JA015540

Zmuda, A. J., Martin, J. H., & Heuring, F. T. (1966). Transverse magnetic disturbances at 1100 kilometers in the auroral region. *Journal of Geophysical Research*, *71*(21), 5033–5045. https://doi.org/10.1029/JZ071i021p05033